# Design of a Photonic Crystal Planar Luneburg Lens for Optical Beam Steering

by

Samuel Kim

B.A. Physics
Harvard University, 2015

Submitted to the
Department of Electrical Engineering and Computer Science
in Partial Fulfillment of the Requirements for the Degree of
Master of Science in Electrical Engineering and Computer Science
at the
Massachusetts Institute of Technology
June 2019



Signature redacted

Signature of the author: _____
Department of Electrical Engineering and Computer Science
April 26, 2019

Signature redacted

Certified by: _____
Marin Soljačić
Professor of Physics
Thesis Supervisor

Signature redacted

Accepted by: _____
Leslie A. Kolodziejski
Professor of Electrical Engineering and Computer Science
Chair, Department Committee on Graduate Students

# Design of a Photonic Crystal Planar Luneburg Lens for Optical Beam Steering

by

Samuel Kim

Submitted to the Department of Electrical Engineering and Computer Science
on April 26, 2019 in Partial Fulfillment of the
Requirements for the Degree of
Master of Science in Electrical Engineering and Computer Science

ABSTRACT

Optical beam steering has numerous applications including light detection and ranging (LIDAR) for three-dimensional (3D) sensing, free space communications, additive manufacturing, and remote sensing. In particular, there is an increasing demand for LIDAR in a variety of applications including autonomous vehicles, unammaned aerial vehicles (UAVs), robotics, and remote sensing. Ideal solutions are small in size, weight, and power consumption (SWaP) while maintaining long range, high resolution, and large field of view (FOV).

Here I present a design for a planar Luneburg lens for use in a silicon photonics optical beam steering device fabricated using CMOS-compatible techniques. The gradient index of the lens is achieved using a photonic crystal consisting of amorphous silicon patterned with a triangular lattice of holes layered on top of silicon nitride. Multiple waveguides can be placed along the focal circle of the lens and the lens is designed to collimate the beam from the waveguides. Through full-wave simulations, the lens is shown to be diffraction-limited with a beamwidth of 0.55° for a lens with radius $R = 100\,\mu m$. The lens is also studied for robustness to fabrication variations. The lens would allow a solid-state on-chip optical beam steering device with a FOV of 160° with no off-axis aberrations.

Thesis Supervisor: Marin Soljačić

Title: Professor of Physics

# Acknowledgements

I would like to first acknowledge my research supervisor, Professor Marin Soljačić, for his continuous support of my research. He has allowed me to work as independently as possible while also keeping his door open to me to talk about anything ranging from tackling specific technical challenges in my work to approaching my career goals. He is an inspiring scientist and advisor who pushes me to be successful.

I would also like to thank everyone with whom I have had the pleasure to work with on this project. Professor Steven Johnson has taught me a tremendous amount on the beauty of photonic crystals, and he and Professor George Barbastathis have provided insightful comments on how to approach this project during its early stages. I am grateful for my entire research group for their support both technically and personally, and for providing a collaborative and fun environment to work in. In particular, I would like to thank Josué López and Jamison Sloan who have been working on related projects before I started this work. They got me up to speed and worked closely with me on pushing this project forward.

Finally, I am grateful for my family and friends including my blockmates from college and my friends here at MIT. They have all supported me throughout the years and pushed me to pursue my passions and go as far as possible. Without them I would not have pursued this path.

# Contents

**1 Introduction** **13**

**2 Luneburg Lens Theory** **17**

**3 Lens Implementation** **23**

3.1 Materials and Fabrication . . . . . 24

3.2 Photonic Crystals . . . . . 24

3.3 Photonic Crystal Lens . . . . . 30

3.4 Other Photonic Crystals . . . . . 31

**4 Methods for Lens Simulation** **35**

**5 Results** **39**

5.1 Lens Performance . . . . . 39

5.2 Robustness to Fabrication . . . . . 48

**6 Conclusion and Outlook** **53**

# List of Figures

1.1 Architecture of lens-based chip-scale LIDAR system. Figure from [30] ©2017 MIT. . . . . 15

2.1 Ray tracing of the Luneburg lens in normalized coordinates such that the radius of the lens is $R = 1$. The Luneburg lens focuses two spheres concentric with the lens onto each other. In this example, the conjugate focal spheres have radii $r_0 = \infty$ and $r_1 = s$ such that rays emanating from a point source are collimated by the lens. . . . . 17

2.2 Luneburg lens normalized refractive index as a function of normalized radius. (a) Original Luneburg formulation for fixed $r_0 = \infty$ and various $r_1 = s$. (b) Generalized formulation with an outer shell of constant index $n_c$, $r_0 = \infty$, and $r_1 = 2$. $n_c = 1$ is equivalent to the original Luneburg formulation. Note that setting $n_c > 1$ increases the maximum refractive index required but also decreases the range of the refractive index required. . . . . 19

3.1 (a) 3D Schematic of the photonic crystal consisting of a layer of a-Si with a triangular lattice of holes sitting on a layer of SiN. The a-Si and SiN layers have thicknesses $t$ and 200 nm, respectively. (b) Top view of the photonic crystal. The lattice has periodicity $a$ and the holes have diameter $d$. . . . . 25

3.2 Reciprocal lattice of the triangular lattice. The dotted line represents the Brillouin zone and the shaded triangle represents the irreducible Brillouin zone. The corners of the irreducible Brillouin zone are denoted as the Γ, K, and M points. . . . . 26
3.3 Wavelength and thickness dependence of refractive index of a-Si layer. . . . . 27
3.4 Dependence of the refractive index of the photonic crystal as a function of $t$ and $d$. . . . . 28
3.5 Anisotropy of the photonic crystal as measured by the ratio of the effective indices at the K and M points in (a) 3D and (b) 2D. . . . . 28
3.6 Validity of the effective index approximation of the photonic crystal as measured by the ratio of phase to group index in (a) 3D and (b) 2D. . . . . 29
3.7 (a) Luneburg lens index profile for $s = 2.8$ (blue) and the effective index achieved by the photonic crystal (orange). (b) Photonic crystal $d$ as a function of lens radius to achieve the Luneburg lens index profile. . . . . 30
3.8 Photonic crystal implementation of the Luneburg lens with $R = 10\,\mu\text{m}$. Black represents the a-SI slab while white represents the SiN slab. (a) $s = 2.8$. The index profile is shown in Figure 3.7. Note the region in the center of the lens where $d = 0\,\mu\text{m}$ and it is a solid a-Si slab. (b) $s = 5$. The dotted line represents the desired perimeter of the lens, but the desired the index is too low to achieve with the photonic crystal and so the lens region is truncated. 31
3.9 (a) Cross and (b) 3-stepped cross shapes for a triangular lattice. The crosses are inscribed in a regular hexagon (inner dotted line) which is concentric with and oriented the same way as the hexagonal unit cell that it lies in (outer dotted line). The dimensions of the crosses are determined by a single parameter, $d$. . . . . 32

3.10 (a) Ratio $n_{cross}/n_{hole}$ where $n_{cross}$ and $n_{hole}$ are the refractive indices of the cross and circular hole-based photonic crystals, respectively. (b) Ratio $n_{cross}/n_{hole}$ where $n_{cross}$ and $n_{hole}$ are the refractive indices of the 3-stepped cross and circular hole-based photonic crystals, respectively. . . . . 32

3.11 Anisotropy of the photonic crystal as illustrated by the ratio $n_M/n_K$ for (a) the cross photonic crystal and (b) the 3-stepped cross photonic crystal. . . . 33

4.1 (a) Permittivity profile of the 2D simulation in MEEP. Black is a-Si, grey is SiN, and white is $SiO_2$. (b) Resulting magnetic field, $H_z$ of the MEEP simulation. . . . . 36

4.2 Farfield plots for a lens with radius $R = 30\,\mu m$. (a) Polar plot of the farfield in the SiN slab. (b) Farfield corrected for air and zoomed into the main lobe. 37

5.1 Simulation of the lens (gray) with a plane wave sent in from the right so that we can see focusing. (a) $H_z$ profile (red and blue). (b) Time-averaged magnetic field energy density, $\mu_0|\mathbf{H}|^2/2$ (orange). . . . . 40

5.2 Results of sending in a plane wave into the lens and measuring the focused field. (a) Error in the focal length measured by the location of the maximum field. (b) Resolution criterion of the focused field as measured by the distance from the maximum field to the first minimum, $\delta$, and the analytical solution for the Rayleigh diffraction limit. The points for $R = 50\,\mu m$ and $R = 100\,\mu m$ are overlayed on each other and thus cannot be seen separately. . . . . 40

5.3 $H_z$ (red and blue) overlayed on the permittivity profile (greyscale) of a simulation of a dipole source and an ideal lens with $s = 2$ and $R = 25\,\mu m$. . . . . 42

5.4 Far field FWHM of the collimated beam using an ideal lens and both a dipole source and waveguide (WG) source. The dotted line is the analytical FWHM assuming a uniformly illuminated aperture, which results in a sinc function pattern in the farfield. . . . . 42

5.5 Behavior of a waveguide mode traveling from a waveguide into a waveguide slab. (a) $H_z$ (b) Streamlines of the time-averaged Poynting vector, $\mathbf{S}$. Only vectors above an aribtrary threshold are plotted to better visualize the beam in the lab. The point at which the waveguide meets the slab waveguide is at $x = 0$. . . . . 43

5.6 The predicted focal point at each $y_i$ along several slices in $x_i$. . . . . 44

5.7 Effect of photonic crystal periodicity. Lens simulation with (a) $a = 300\,\text{nm}$, (b) 400 nm, and (c) 500 nm. . . . . 45

5.8 Far field of photonic crystal lens and idealized lens for $R = 30\,\mu\text{m}$. . . . . 46

5.9 (a) Far field of the photonic crystal lens for various radii. (b) FWHM of the photonic crystal lens, idealized lens, and idealized lens illuminated by a dipole source for various lens radii. For reference the analytical FWHM of an Airy disk profile and a Gaussian beam are also plotted. . . . . 46

5.10 Far field of photonic crystal lens as a function of lens rotation. . . . . 47

5.11 Measuring robustness to fabricated a-Si thickness, where the designed a-Si thickness is $t = 30\,\text{nm}$. . . . . 48

5.12 Measuring robustness to fabricated a-Si thickness, where the designed a-Si thickness is $t = 30\,\text{nm}$ and there are 64 ports. . . . . 49

5.13 Robustness of the lens performance to the hole size by applying Gaussian noise $\epsilon_d \sim \mathcal{N}(\mu_d, \sigma_d)$ to the hold size as $d' = d + \epsilon$. This is measured fractional change of the FWHM with respect to the unperturbed lens as a function of (a) $\mu_d$ for $\sigma_d = 10$ (the dotted line represent the case where $\mu_d =$ and $\sigma = 0$ and (b) $\sigma_d$ for $\mu_d = 0$. . . . . 49

5.14 Robustness of the lens performance to the hole location by applying Gaussian noise $\epsilon_r \sim \mathcal{N}(\mu_r, \sigma_r)$ to the coordinates of each hole as $x' = x + \epsilon_r$ and $y' = y + \epsilon_r$. Set $\mu_r = 0$. This is measured as the fractional change of the FWHM with respect to the unperturbed lens. . . . . 50

# Chapter 1

# Introduction

Optical beam steering consists of actively controlling the direction of a laser beam over a range of angles. It has numerous applications [1, 2] including light detection and ranging (LIDAR) for mapping and navigation [3], free-space optical communications, projection [4], and additive manufacturing.

In LIDAR, a three-dimensional (3D) map of an environment or remote object is constructed by sending out a pulsed laser light at various angles and measuring the reflected pulse. Analagous to radar, LIDAR uses the return time and wavelength of the reflected light to compute the distance and relative velocity at each direction in space. The number of received photons can also be used to measure reflectance of the surface. LIDAR has long been used for creating detailed 3D maps of terrains for construction [5], mining [6], agriculture [7], archaeology [8], environmental science (e.g., flood mapping, forestry, vegetation mapping, erosion of sandy beaches) [9], and many more applications. More recently, commercial interest in more portable LIDAR has increased dramatically for applications in self-driving vehicles [10], autonomous robots [7], and unmanned aerial vehicles (UAVs) [11].

Free-space optical communications encodes information in a modulated light pulse to wirelessly send information to a remote receiver and is useful in scenarios where physical connections are impractical such as communications with vehicles, aircraft, or spacecraft. It

is also attractive because the bandwidth of optical communications is orders of magnitude greater than that of radio-frequency (RF) communications. While optical communications typically uses LEDs as the light source, there is large interested in using a steered laser beam to improve efficiency, range, and security [12].

With increasing use of robots, vehicles, and drones, there is also increasing interest in LIDAR or free-space optical communications devices that are suited for these platforms. These applications requires low weight, size, power, and cost (SWAP-C) while maintaining performance metrics such as range, resolution, scan rate, and field of view (FOV). Because these platforms are moving and often undergo harsh conditions, they require high reliability and robustness. Additionally, the increasing commercial interest in LIDAR requires future solutions to be more scalable. All of these factors drive towards solid-state on-chip solutions for optical beam steering [13].

Current commercial solutions for optical beam steering typically use lasers that are mounted on a rotating stage or stationary lasers that are redirected using a moving mirror, lens, prism, or diffraction grating. However, the moving parts make these solutions bulky, heavy, power-hungry, difficult to mass manufacture, and unreliable. There have been a number of solid-state solutions for optical beam steering that do not use moving parts, although they all currently face tradeoffs in the aforementioned factors. A tunable spatial light modulator (SLM) using liquid crystals as the tunable element can be used as a passive optical phased array (OPA) where the liquid crystal controls the phase of a reflected or transmitted beam at each point in space, thus tuning the direction of the reflected or transmitted beam [1, 13, 14, 15, 16]. Metasurfaces that are actively controlled through electronically tunable materials such as vanadium oxide can be used in a similar manner to redirect the phase front of a transmitted beam through the metasurface [17]. Microelectromechanical systems (MEMS) optical beam steering typically consists of actuated mirrors fabricated on a silicon chip to steer a beam [18, 19, 20, 21, 22]. MEMS offers greater reliability and smaller SWAP-C characteristics than macro-mechanical solutions because of the on-chip integration,

but it is not truly solid-state because of the moving parts and so it still suffers from sensitivity to vibrations. Active OPAs use an array of optical antennas that are actively controlled in phase to steer the outgoing beam [2, 3, 4, 23, 24, 25, 26, 27]. Active OPAs are attractive because of their fully integrated and solid-state design but still suffer from limited FOV due to sidelobes and have high complexity of phase controls. Another solution uses discrete switching between different waveguides combined with a 3D lens for beam steering, although this is not on-chip and would require an extra alignment step in manufacturing [28, 29].

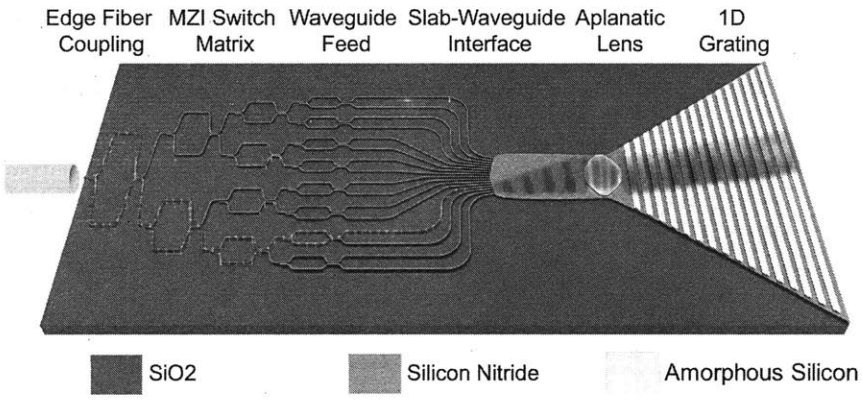


Figure 1.1: Architecture of lens-based chip-scale LIDAR system. Figure from [30] ©2017 MIT.

An alternative architecture for chip-scale LIDAR has been proposed [30] and experimentally demonstrated [31] to address the shortcomings of other optical beam steering solutions, and a schematic of the architecture is shown in Figure 1.1. In this architecture, a tunable laser source centered at 1550 nm couples into an on-chip waveguide made of silicon nitride (SiN) encapsulated in silicon dioxide ($SiO_2$). The waveguide feeds into a switch matrix composed of Mach-Zehnder interferometers that can route the signal into one of $N$ waveguide ports. The waveguide ports feed into a SiN slab at different azimuthal (in-plane) angles, where an aplanatic lens consisting of amorphous silicon (a-Si) layered on top of SiN collimates the beam from each port. Thus, by switching the port that the signal routes through, this architecture can change the in-plane angle of the collimated beam. Finally, a grating consisting of a-Si rulings on top of SiN scatters the beam out of plane. By tuning the wavelength of the source, one can change the out-of-plane angle, thus enabling two-dimensional

(2D) beam steering.

This architecture has much lower power consumption than OPAs due to the need to control only $\mathcal{O}(\log_2 N)$ switches at a time as opposed to $\mathcal{N}$ phase tuners for OPAs. It also has the advantage of reduced thermal management, simpler control systems, and robustness to environmental factors. However, this architecture has an azimuthal FOV of $\pm 20°$ due to off-axis aberrations of the lens, which limits its applications. There are a number of wide angle lens designs with FOV up to 190°, but these suffer from asymmetric behavior of the entrance pupil and aperture size as one moves off-axis [32] which would reduce performance off-axis and make the following grating more difficult to design.

Here, I propose a new lens design based on the Luneburg lens that has a theoretical FOV of 360°. The Luneburg lens is a spherically symmetric lens that maps two spheres onto each other. It is a gradient-index (GRIN) lens in that the index of refraction smoothly varies across the lens. Here, a photonic crystal is used to realize the gradient index of the lens. The lens is designed within the constraints of CMOS-compatible fabrication techniques. Full-wave electromagnetic simulations are used to predict the behavior of the lens as well as study the robustness of the lens to variations in fabrication.

# Chapter 2

# Luneburg Lens Theory

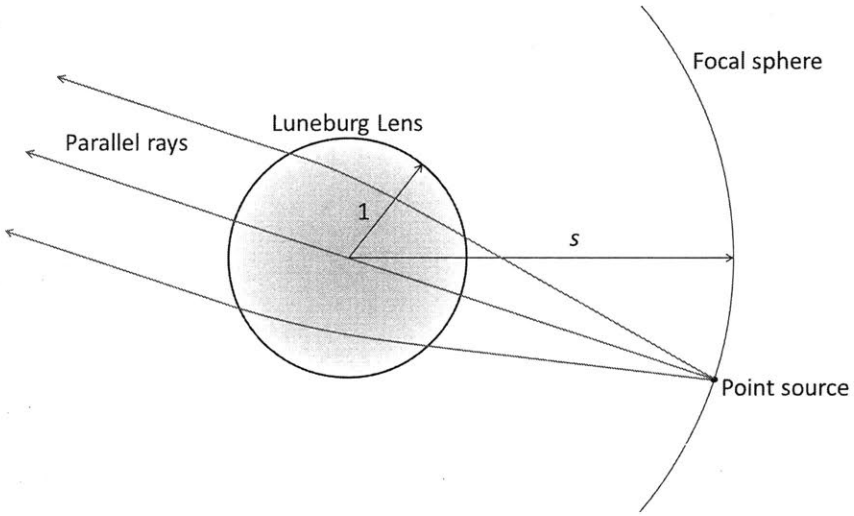


Figure 2.1: Ray tracing of the Luneburg lens in normalized coordinates such that the radius of the lens is $R = 1$. The Luneburg lens focuses two spheres concentric with the lens onto each other. In this example, the conjugate focal spheres have radii $r_0 = \infty$ and $r_1 = s$ such that rays emanating from a point source are collimated by the lens.

The Luneburg lens is a spherically symmetric gradient-index lens that focuses two spheres concentric with the lens onto each other, where the focal spheres have radii equal or greater than that of the lens as shown in Figure 2.1 [33]. For example, in the case where the object sphere has radius $r_0 = \infty$ and image sphere has radius $r_1 = R$ where $R$ is the radius of the lens, then parallel rays coming from any direction focus onto a point on the surface of the lens opposite of the incoming rays. Vice versa, rays emanating from a point source on the

surface of the lens will be collimated by the lens on the opposite side of the lens from the point source. As opposed to traditional lenses that use a single material with a constant index of refraction, the index of refraction of the Luneburg lens $n(r)$ varies smoothly as a function of the radial position $r < R$ inside the lens, thus making it a gradient-index lens. The gradient index causes the rays to bend inside the lens, enabling focusing.

For simplicity in this discussion, assume that $n(r)$ is normalized by the index of the surrounding medium, $n_0$, and that radial quantities ($r$, $r_0$, and $r_1$) are normalized to $R$. For the case where $r_0 = \infty$ and $r_1 = 1$, Luneburg presented the simple solution

$$n(r) = \sqrt{2 - r^2} \tag{2.1}$$

While this case permits a simple analytical solution, it is not ideal for our application of an on-chip planar lens. First, the index variation is too high to achieve with our materials as it requires a maximum index contrast of $\sqrt{2} - 1 \approx 41\%$. For reference, the 2D effective index of the SiN slab with thickness 200 nm is 1.584 and the effective index of a-Si with thickness 30 nm on top of the SiN slab waveguide is 1.775, giving an available index contrast of 12%. Second, the beam exiting the waveguides into the SiN slab has a beam divergence angle of 13.5° [30], which would not use the full aperture of the lens. The reduced aperture of the exiting beam would increase the beam divergence in the far-field and reduce performance.

Thus, we look for solutions for the case where $r_1 \neq 1$. The scenario where $r_0 = \infty$ and $r_1 = s > 1$ is shown in Figure 2.1. Luneburg derived a general solution for the index profile:

$$n = \exp\left[\omega(\rho, r_0) + \omega(\rho, r_1)\right]$$

$$\rho = nr \tag{2.2}$$

$$\omega(\rho, s) = \frac{1}{\pi} \int_{\rho}^{1} \frac{\arcsin\left(\frac{\kappa}{s}\right)}{\sqrt{(\kappa^2 - \rho^2)}} \, \mathrm{d}\kappa, \quad 0 \leq \rho \leq 1, \quad s \geq 1 \tag{2.3}$$

In the case where $r_0 = \infty$ and $r_1 = 1$, this reduces to the explicit expression in Equation

(2.1). Otherwise, this is a transcendental equation without closed-form solutions so solutions must be solved numerically. Additionally, solutions are not unique, which gives us flexibility to find a solution that accomodates fabrication constraints. Fixing $r_0 = \infty$, solutions for various $r_1 = s$ are shown in Figure 2.2(a). Note that fixing $r_0 = \infty$ simplifies Equation (2.3) to:

$$\omega(\rho, \infty) = 0$$

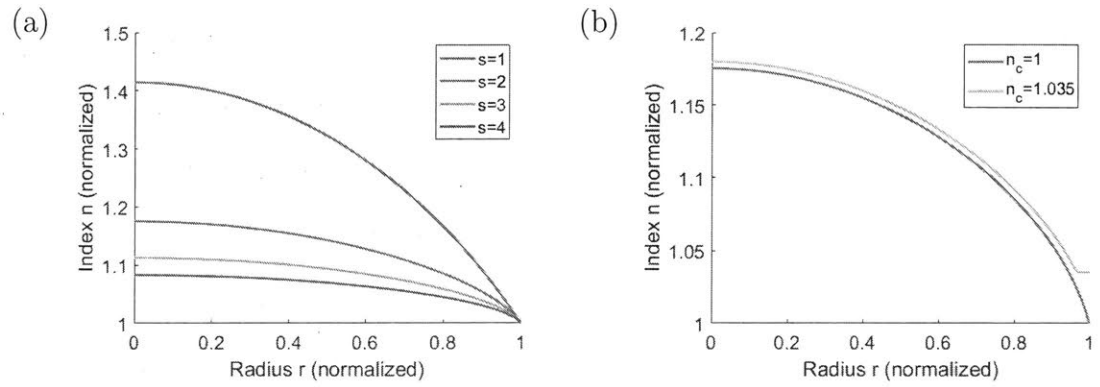


Figure 2.2: Luneburg lens normalized refractive index as a function of normalized radius. (a) Original Luneburg formulation for fixed $r_0 = \infty$ and various $r_1 = s$. (b) Generalized formulation with an outer shell of constant index $n_c$, $r_0 = \infty$, and $r_1 = 2$. $n_c = 1$ is equivalent to the original Luneburg formulation. Note that setting $n_c > 1$ increases the maximum refractive index required but also decreases the range of the refractive index required.

The original formulation of the index profile derived by Luneburg sets $n(1) = 1$ such that the index at the surface of the lens matches that of the surrounding medium. In this case, the lens and surrounding medium are index-matched and there are minimal reflections off of the surface of the lens. There also exist generalizations of the Luneburg lens in which the index is not necessarily smoothly varying and may have discontinuities or where the index at the edge of the lens does not match the index of the surrounding material [34]. In particular, consider the case where the lens can have an outer shell with a specified index profile. The index of the lens inside the shell can then be solved under the constraints of the outer shell.

The index profile is modified to:

$$n = \frac{1}{a}\exp\left[\omega(\rho, r_0) + \omega(\rho, r_1) - \Omega(\rho)\right]$$
$$\Omega(\rho) = \frac{2}{\pi}\int_a^1 \arctan\left(\frac{1-\rho^2}{P^2(r)-1}\right)^{1/2}\frac{\mathrm{d}r}{r} \tag{2.4}$$

where $a < 1$ is the radial distance that separates the inner core and the outer shell and $P(r)$ defines $\rho(r)$ in the outer shell. $\rho$ and $\omega(\rho, s)$ are defined as in Equations (2.2) and (2.3) respectively.

Additionally, consider a lens which has an outer shell with a constant index of refraction $n_c$. Suppose the index profile is continuous at the transition radius $r = a$. Then this gives in the outer shell $a \leq r \leq 1$:

$$\begin{aligned} P(r) &= r/a \\ n_c &= 1/a \end{aligned} \tag{2.5}$$

Additionally, Equation (2.4) simplifies to:

$$\Omega(\rho) = 2\left(\omega(\rho, an_c) - \omega(\rho, n_c)\right)$$

This results in an upper limit on the index $n_c$. If $r_0 = \infty$ and $r_1 = s$, then this upper limit is:

$$n_c \leq \sqrt{2s\left(s - \sqrt{s^2-1}\right)} \tag{2.6}$$

which also imposes an upper limit on the thickness of the outer shell through Equation (2.5).

The lens index profile for this case is shown in 2.2(b). It turns out that with a homogeneous outer shell, although the maximum index of the lens increases and the lens is no longer impedance-matched to the environment, the range of $n(r)$ decreases. This is more amenable in the case where the available material to construct such a lens can only achieve

a limited range of $n$, as is the case with our photonic crystals.

Finally, note that Equation (2.3) as formulated by Luneburg has a singularity in the integral at $\kappa = \rho$. While the integral does not diverge, the transcendental equations are solved for numerically and it can be troublesome to evaluate Equation (2.3) through numerical techniques without special care. Southwell uses a change of variables to remove the singularity and present an alternative version of $\omega(\rho, s)$ that, while seems more complex, is numerically easier to solve [35]:

$$\omega(\rho, s) = \frac{1}{\pi}\left\{2\arcsin\left(\frac{1}{s}\right)\sqrt{\frac{1-p}{1+p}} - \int_0^{1-\rho}\left[\frac{2}{\sqrt{s^2-(y+\rho)^2}} - \frac{\arcsin\left(\frac{y+\rho}{s}\right)}{y+2\rho}\right]\sqrt{\frac{y}{y+2\rho}}\,\mathrm{d}y\right\}$$

Because we are interested in collimating a beam from a source, I set $r_0 = \infty$ and for simplicity rename the focal length $r_1 = s$. The generalized Luneburg lens index profile is used with an outer shell at the upper limit of $n_c$ shown in Equation (2.6). $s$ can be optimized to fit the parameters of the architecture, and the challenge then becomes how to implement the gradient-index lens.

# Chapter 3

# Lens Implementation

As the goal is to design a lens for optical beam steering using an integrated silicon platform, we must design an implementation of the lens subject to fabrication constraints. GRIN lenses such as the Luneburg lens are difficult to implement in practice because of the need for a continuous range of refractive indices, which is not available in natural materials.

In microwave frequencies, Luneburg lenses have been implemented using discrete shells of different materials to approximate the gradient-index [36, 37, 38, 39, 40, 41].

Planar Luneburg lenses have been design and demonstrated for integrate optics by thermal evaporation [42] or sputtering [43] on glass, where the gradient index is realized through varying the thickness of the deposited material. Similar lenses have been demonstrated on silicon photonics platforms using sputtering [44, 45], focused ion beam [46], and grey-scale lithography [47].

Another way to implement GRIN lenses is through metamaterials and photonic crystals, which are periodic structures with periodicity smaller than or comparable to the wavelength of light $\lambda$. By slowly varying unit cell of the periodic structure, one can vary the effective index across the structure and realize a GRIN lens. Graded photonic crystals to implement the Luneburg lens have been analyzed [48, 49, 50, 51, 52] and experimentally demonstrated using electron beam lithography [53]. However,electron beam lithography is expensive and

not scalable. Thus, we explore the implementation of a Luneburg lens constrained by scalable fabrication techniques using photonic crystals.

## 3.1 Materials and Fabrication

In particular, low pressure chemical vapor deposition (LPCVD) is a CMOS-compatible and scalable fabrication technique that can pattern silicon nitride ($Si_3N_4$ or SiN) and amorphous silicon (a-Si).

Silicon nitride is becoming a choice material for photonics due to its low loss at visible to infrared wavelengths and its ability to handle high power [54, 55] compared to silicon-on-insulator (SOI). The index of refraction of SiN is 1.996 at a wavelength of 1.55 µm and deviates less than 0.1% in the wavelength range 1.5 µm to 1.6 µm [56]. The thickness of SiN is assumed to be 200 nm.

Additionally, a-Si can be patterned on top of the SiN layer, and we refer to this stack as the "a-Si slab." I assume that the thickness of a-Si can range 20 nm to 40 nm, although the actual fabricated thickness can vary from the desired thickness. This effect is explored in the Results section. The refractive index of a-Si is taken to be 3.48 [57]. The SiN and a-Si are surrounded by a silicon dioxide ($SiO_2$) cladding, which has a refractive index of 1.44. Because of the higher index of SiN relative to $SiO_2$, we can create a waveguide using SiN. The minimum feature size and minimum gap size of a-Si are assumed to be 100 nm.

## 3.2 Photonic Crystals

Metamaterials and photonic crystals are periodic structures with periodicity smaller than or comparable to the wavelength of light, $\lambda$, and thus cannot be analyzed directly using common approximations such as ray optics which assume that $\lambda$ is significantly smaller than all physical features of the system. The periodicity of metamaterials is typically less than $\sim \lambda/10$, which allows them treated with an effective index of refraction [58, 59] and achieve

refractive indices not found in natural materials, including negative index of refraction [60]. Photonic crystals are typically dielectric structures with periodicity on the order of $\lambda/2$ that can be designed to display a wide variety of fascinating optical phenomena that do not exist in natural materials [61] such as supercollimation [62] and the superprism effect [63].

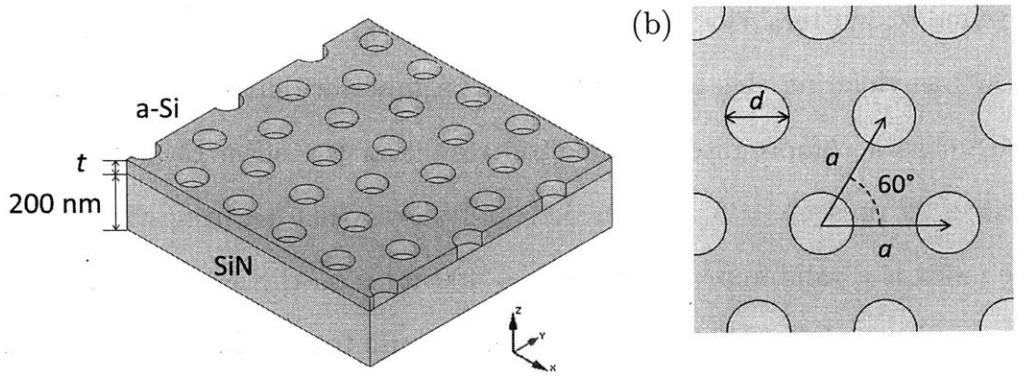


Figure 3.1: (a) 3D Schematic of the photonic crystal consisting of a layer of a-Si with a triangular lattice of holes sitting on a layer of SiN. The a-Si and SiN layers have thicknesses $t$ and 200 nm, respectively. (b) Top view of the photonic crystal. The lattice has periodicity $a$ and the holes have diameter $d$.

Here we consider the effective index of such a periodic structure. By slowly varying the unit cell of the periodic structure across the material, one can vary the effective index across the structure and realize a GRIN lens. This relies on the assumption that the unit cell is varying slowly enough such that the structure is still approximately locally periodic and thus can be treated as a metamaterial or photonic crystal at each point in the material. The structure used to implement the Luneburg lens, which we refer to as a photonic crystal, is a triangular lattice of holes in amorphous silicon (a-Si) layered on top of a solid 200 nm layer of silicon nitride (SiN) encapsulated in $SiO_2$. The a-Si layer has a thickness of $t$ =20 nm to 40 nm, where $t$ is fixed for a particular implementation of the Luneburg lens and can be optimized. The triangular lattice has periodicity $a$ and the hole has diameter $d$. A schematic of the photonic crystal is shown in Figure 3.1.

The periodicity $a$ has to be carefully chosen to optimize for performance while taking into account fabrication constraints. The smallest hole diameter achievable is $d_{min} = 100$ nm based on the minimum gap size, and the largest hole diameter achievable is $d_{max} = a -$

100 nm based on the minimum feature size. A small periodicity ensures that the unit cells are sufficiently sub-wavelength such that we can accurately treat the material using an effective index, but it limits the range of achievable refractive index due to limitations on the rnage of achievable hole diameters. A larger periodicity allows a greater range of achievable refractive index, but may violate the effective index approximation, and is ultimately limited by $a < \lambda/2$ as violating this limit would cause significant diffractive effects. Thus, I choose $a = 400\,\text{nm}$ as a compromise. Simulation results of the effect of periodicity on the lens performance is presented in Section 5.1, and shows that treating the structure with an effective index is a valid approximation. $a = 400\,\text{nm}$ is on the order of $\sim \lambda/2$, and so I refer to our material as a photonic crystal although we use the effective index approximation, as the distinction between metamaterials and photonic crystals can be quite nebulous.

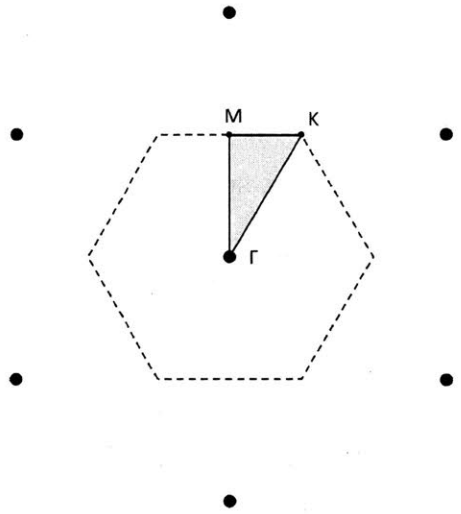


Figure 3.2: Reciprocal lattice of the triangular lattice. The dotted line represents the Brillouin zone and the shaded triangle represents the irreducible Brillouin zone. The corners of the irreducible Brillouin zone are denoted as the Γ, K, and M points.

It is convenient to deal with the effective 2D properties because we are only considering guided modes inside either the waveguide or the slab. To do this, I simulate the electromagnetic behavior of the waveguide slabs and the photonic crystal using an open-source software package, MPB [64]. MPB uses frequency-domain methods to solve Maxwell's equations to find the modes of a structure at a given wavevector $\vec{k}$. Because the boundary conditions in

MPB simulations are periodic, space is added in the $\pm z$ directions of the simulation such that the guided mode has decayed sufficiently away from the waveguide slab or photonic crystal. The reciprocal lattice of the triangular lattice is shown in Figure 3.2. Along each of the edges of the irreducible Brillouin zone, I extract the dispersion $\omega(k)$ of the photonic crystal as a function of $k = |\vec{k}|$, the wavenumber. An effective index of refraction is calculated using the relation $n_{eff} = \frac{ck}{\omega(k)}$ where $c$ is the speed of light. This is also known as the phase index since it is calculated using the phase velocity $v_p = \frac{\omega(k)}{k}$. Unless otherwise specified, assume that $n_{eff}$ and $v_p$ are extracted along the $\Gamma - \mathrm{M}$ edge of the Brouillin zone, although we will see shortly that this choice does not have a large impact.

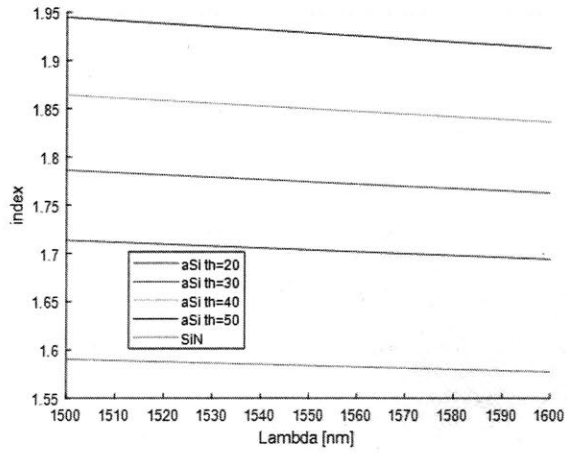


Figure 3.3: Wavelength and thickness dependence of refractive index of a-Si layer.

I use the TE mode (where the magnetic field is pointing out of plane, i.e., $E_z = 0$ and $H_x = H_y = 0$). This mode is the fundamental mode of the waveguide. Because the electric field is in plane, this mode also maximizes the index contrast between SiN and a-Si, giving us a greater index contrast and thus a greater range of the refractive index. For the waveguide slabs, the effective indices of SiN and a-Si are shown in Figure 3.3 as a function of wavelength and a-Si thickness.

By changing $d$ in the photonic crystal, we tune the dispersion $\omega(k)$ and thus the effective index. For periodicity $a = 400\,\mathrm{nm}$, the hole diameter can range from $d_{min} = 100\,\mathrm{nm}$ to $d_{max} = 300\,\mathrm{nm}$. The effective index of the photonic crystal is shown in Figure 3.4 as a

function of $d$ and $t$. Here, I refer to "3D" as simulating the full 3D structure of the photonic crystal unit cell. For comparison, I also analyze the unit cell using 2D simulations where the hole region and a-Si regions use the 2D effective indices of SiN and a-Si slabs, respectively. The 2D effective indices are also shown in Figure 3.4. These are used to build 2D simulations which are more computationally feasible relative to full 3D simulations. The plot of $n_{eff}$ for the 2D dispersion is extended out to $d = 350\,\text{nm}$ so that it contains the full range of $n_{eff}$ of the 3D dispersion.

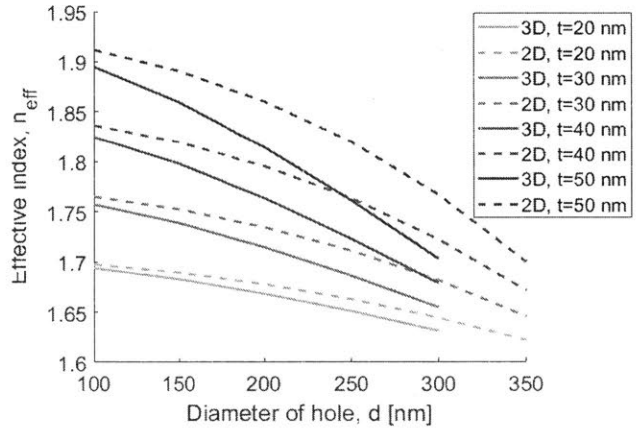


Figure 3.4: Dependence of the refractive index of the photonic crystal as a function of $t$ and $d$.

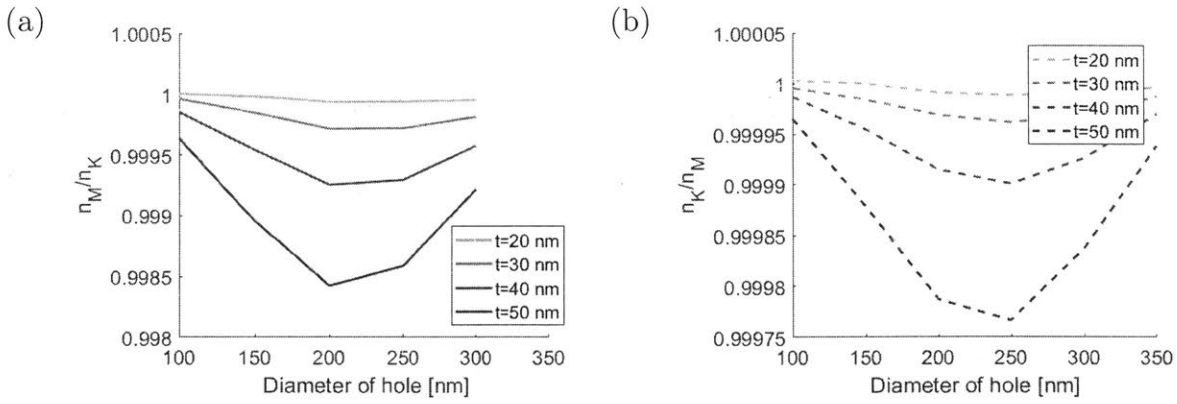


Figure 3.5: Anisotropy of the photonic crystal as measured by the ratio of the effective indices at the K and M points in (a) 3D and (b) 2D.

The triangular lattice was chosen because it has the highest degree of symmetry for 2D lattices and thus minimizes anisotropic behavior. The anisotropy of the photonic crystal

refractive index is illustrated in Figure 3.5(a) through a plot of $n_M/n_K$, where $n_M$ and $n_K$ are the effective indices extracted along the $\Gamma - \mathrm{M}$ and $\Gamma - \mathrm{K}$ edges in the reciprocal lattice. The anisotropy increases with $t$ which is expected since the electromagnetic behavior of the photonic crystal deviates further from that the isotropic SiN slab as $t$ increases. However, the anisotropy is less than 0.2% across all parameter ranges of interest, so we can ignore anisotropic effects in our modeling. The anisotropy of the photonic crystal modeled in 2D is less than 0.03%, so this is a valid substitute model of the 3D system assuming negligible anisotropy.

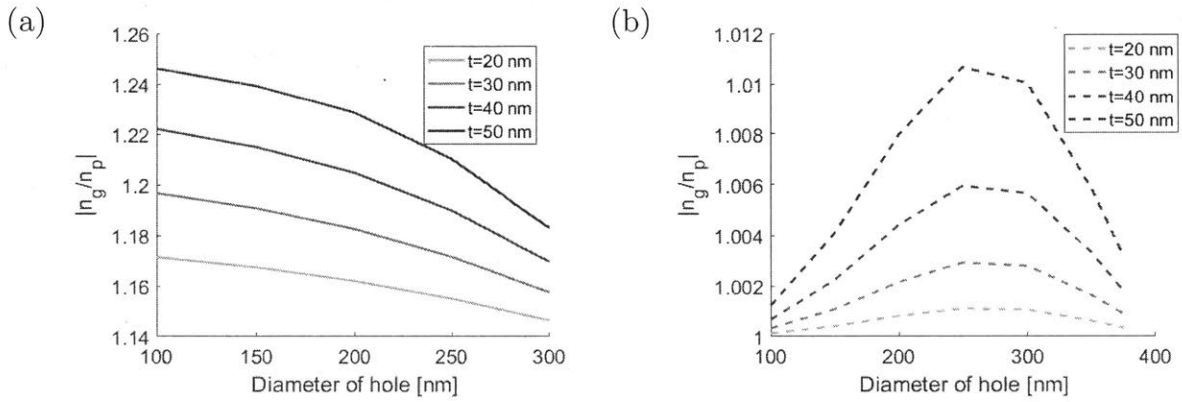


Figure 3.6: Validity of the effective index approximation of the photonic crystal as measured by the ratio of phase to group index in (a) 3D and (b) 2D.

To further validate the assumption of an effective index, I compare the phase index of the photonic crystal to its group index $n_g = \frac{c}{v_g}$ where $v_g = \frac{\partial \omega(k)}{\partial k}$ is the group velocity. In the regime where the use of an effective index is valid, the dispersion should be linear such that $v_p = v_g$ and thus $n_p = n_g$. The ratio $n_p/n_g$ is plotted in Figure 3.6 for both the 3D model and the equivalent 2D model. For the 3D model, the ratio increases with $t$ and is on the order of $\sim 20\%$ which is not negligible. Because we are interested in the lensing behavior, i.e., how the phase front is transformed by the lens, I use the phase index as opposed to the group index for designing the lens. The 2D model shows a relatively small ratio of $\sim 1\%$, so 2D simulations will fail to show the effects of this discrepancy. However, because the lens is such a small structure relative to the entire system (as opposed to a waveguide), the effects

of the group index can be ignored.

## 3.3 Photonic Crystal Lens

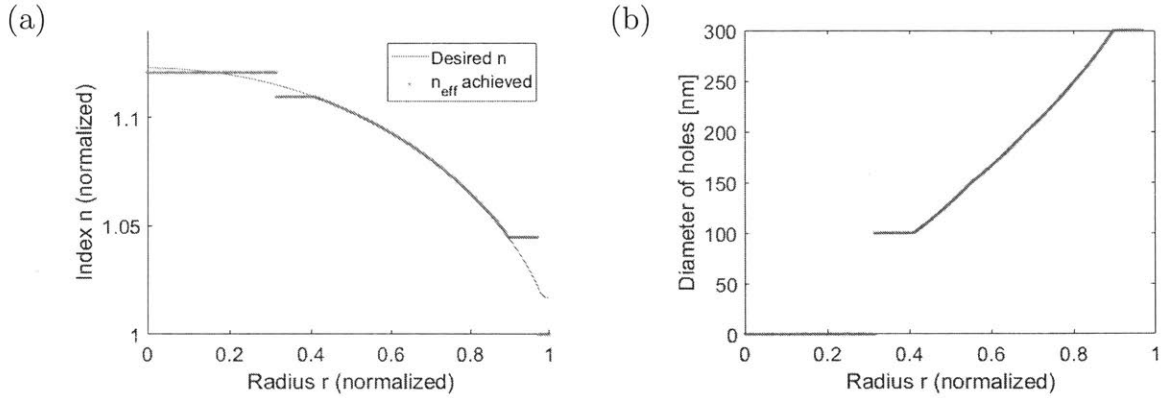


Figure 3.7: (a) Luneburg lens index profile for $s = 2.8$ (blue) and the effective index achieved by the photonic crystal (orange). (b) Photonic crystal $d$ as a function of lens radius to achieve the Luneburg lens index profile.

To build the lens using the photonic crystal, the hole size is slowly varied across the lens to realize the GRIN structure. In particular, a triangular lattice with periodicity $a$ is superimposed on the lens, and at each unit cell in the lattice, the required refractive index of the lens is calculated and the hole size $d$ is determined to match that index. If $d$ required is outside of the range 100 nm to 300 nm, then $d$ is either (1) truncated to the ends of the range 100 nm to 300 nm, (2) set to $d = 0$ nm (solid a-Si slab with no holes), or (3) set to $d = \infty$ (SiN slab without an a-Si layer).

An example of a Luneburg lens index profile with $s = 2.8$ and the realized index profile by the photonic crystal are shown in Figure 3.7(a) and the corresponding $d$ is shown in Figure 3.7(b). We can see for $r < 0.31R$, the desired index profile is too high to achieve for the photonic crystal and so we set $d = 0$ nm (a-Si slab with no hole). In the range $0.31R < r < 0.41R$, the index is approximated with $d = 100$ nm. In the range $0.90R < r < 0.97R$, the index is approximated with photonic crystal of $d = 300$ nm. In the range $r > 0.97R$, the desired index is too low for the photonic crystal and so we set $d = \infty$, which is just the SiN

slab. Because the surrounding medium is also the SiN slab, this is equivalent to truncating the radius of the lens. The resulting lens is shown in Figure 3.8(a). Figure 3.8(b) shows the case for $s = 5$. Note that the lens truncation is more apparent for $s = 5$ because a larger $s$ requires a lower desired index.

(a) (b)

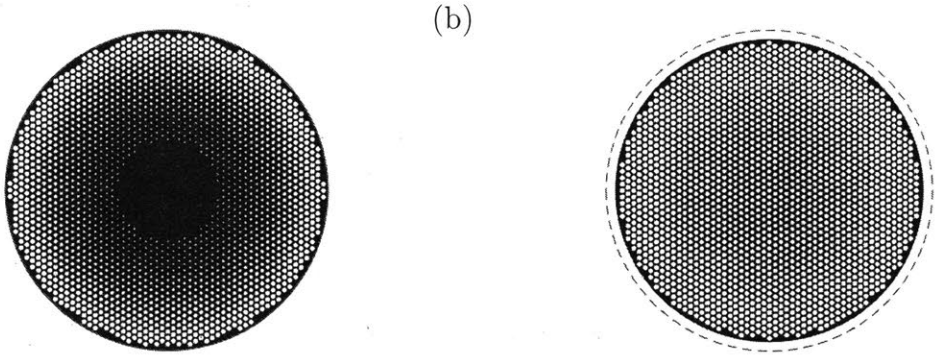

Figure 3.8: Photonic crystal implementation of the Luneburg lens with $R = 10\,\mu\text{m}$. Black represents the a-SI slab while white represents the SiN slab. (a) $s = 2.8$. The index profile is shown in Figure 3.7. Note the region in the center of the lens where $d = 0\,\mu\text{m}$ and it is a solid a-Si slab. (b) $s = 5$. The dotted line represents the desired perimeter of the lens, but the desired the index is too low to achieve with the photonic crystal and so the lens region is truncated.

## 3.4 Other Photonic Crystals

Other photonic crystal structures were considered to implement the GRIN lens. A triangular lattice of posts would achieve a range of refractive indices lower than that of the lattice of holes. Combining both holes and posts would thus achieve a greater total range of refractive indices, giving us greater flexibility in design. However, from a fabrication perspective, it is easier to use just one type of photonic crystal because each type of shape (holes versus posts) needs to be calibrated separately. Thus, for simplicity, we opted to use only a lattice of holes. We will see in the next section that truncating the lower range of effective index does not significantly harm the performance of the lens.

Additionally, while the triangular lattice offers the highest degree out of any 2D regular

lattice and thus minimizes anisotropy, non-regular lattices were also considered including concentric rings of holes or posts and randomized positions of holes or posts. However, while non-regular lattices can decrease anisotropy or reduce unwanted diffraction orders [65], they are often much more complex to design.

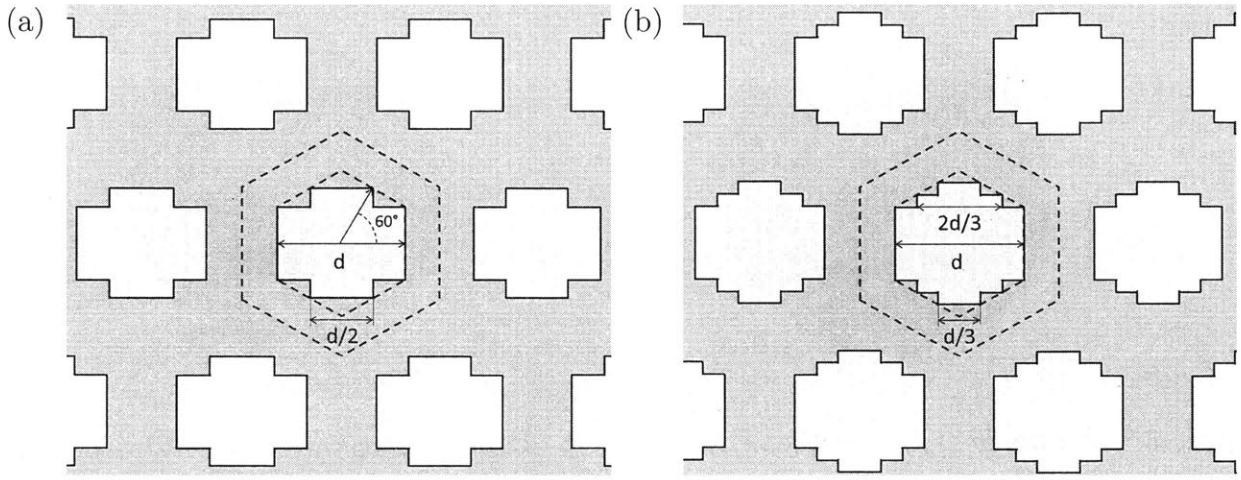


Figure 3.9: (a) Cross and (b) 3-stepped cross shapes for a triangular lattice. The crosses are inscribed in a regular hexagon (inner dotted line) which is concentric with and oriented the same way as the hexagonal unit cell that it lies in (outer dotted line). The dimensions of the crosses are determined by a single parameter, $d$.

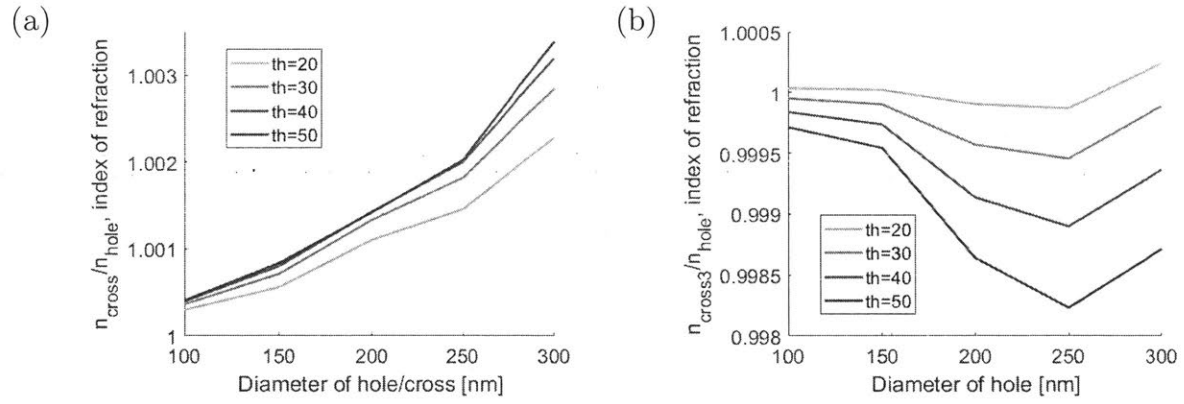


Figure 3.10: (a) Ratio $n_{cross}/n_{hole}$ where $n_{cross}$ and $n_{hole}$ are the refractive indices of the cross and circular hole-based photonic crystals, respectively. (b) Ratio $n_{cross}/n_{hole}$ where $n_{cross}$ and $n_{hole}$ are the refractive indices of the 3-stepped cross and circular hole-based photonic crystals, respectively.

Another photonic crystal structure I considered is a triangular lattice of holes where the holes are not circular, such as crosses or 3-stepped crosses as shown in Figure 3.9. The

boundaries of these unit cells are aligned with the Cartesian coordinates which simplifies the process of physically writing the lithography mask because the laser or electron beam that etches the mask usually travels along the Cartesian coordinates. The size of these non-circular holes is defined by $d$ and can range from $d_{min} = 100\,\text{nm}$ to $d_{max} = a - 100\,\text{nm}$ based on the minimum feature size and minimum gap size. The refractive indices of these alternate photonic crystals is very similar to that of the circular-hole photonic crystal for a given $d$ as shown in Figure 3.10.

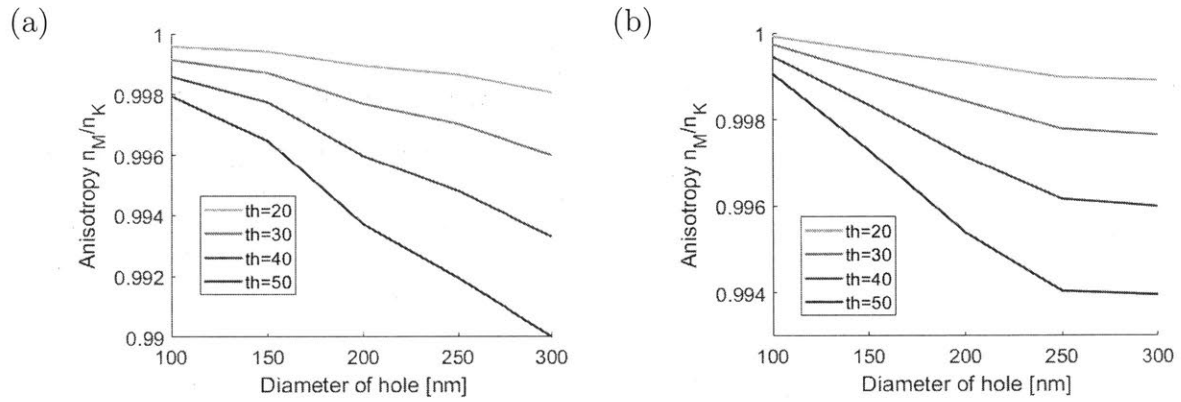


Figure 3.11: Anisotropy of the photonic crystal as illustrated by the ratio $n_M/n_K$ for (a) the cross photonic crystal and (b) the 3-stepped cross photonic crystal.

The anisotropy of these alternate photonic crystals are shown in Figure 3.11. Both structures are more anisotropic than the circular-hole photonic crystal, as suspected, because the new structures reduce the symmetry from 6-fold to 4-fold symmetry. However, the anisotropy is still small enough that it can be safely ignored.

For simplicity of analysis, I implement the lens using the circular-hole photonic crystal. However, as previously stated, the alternate photonic crystals can be simpler and faster to implement in fabrication.

# Chapter 4

# Methods for Lens Simulation

To characterize and optimize the lens performance, simulations of the lens are carried out using the finite-difference time-domain (FDTD) method using MEEP, an open-source software package [66]. MEEP is a full-wave electromagnetic solver that simulates the electromagnetic fields exactly using Maxwell's equations. While ray-tracing is often used to simulate electromagnetic phenomena such as lens behavior, it is only valid in the limit where feature sizes are much larger than the wavelength of light. Photonic crystals by definition have sub-wavelength features and so we must treat it using Maxwell's equations to study the effects of the photonic crystal.

Because full-scale 3D simulations of the lens are prohibitively computationally expensive, 2D simulations are used to simulate the lens. The effective refractive indices of the a-Si and SiN slabs are used in place of the bulk indices for a-Si and SiN. The hole sizes are determined using the 2D effective indices plotted in Figure 3.4 while also being constrained to the index ranges of the 3D structure.

The 2D MEEP simulations implement open boundaries using a perfectly matched layer (PML) with a thickness of 1 µm. The boundaries of the simulation 10 µm away from the edges of the lens. The resolution of the simulation is 30 mesh cells per µm. Increasing these values do not make any appreciable difference to the simulation results. The waveguide that

feeds into the waveguide slab is 5 µm long and 1 µm wide. To accurately represent the source, I take advantage of MPB's integration with MEEP to calculate the fundamental mode of the waveguide, and use a current source that excites this mode. The point at which the waveguide feeds into the waveguide slab is placed at the focal point of the lens.

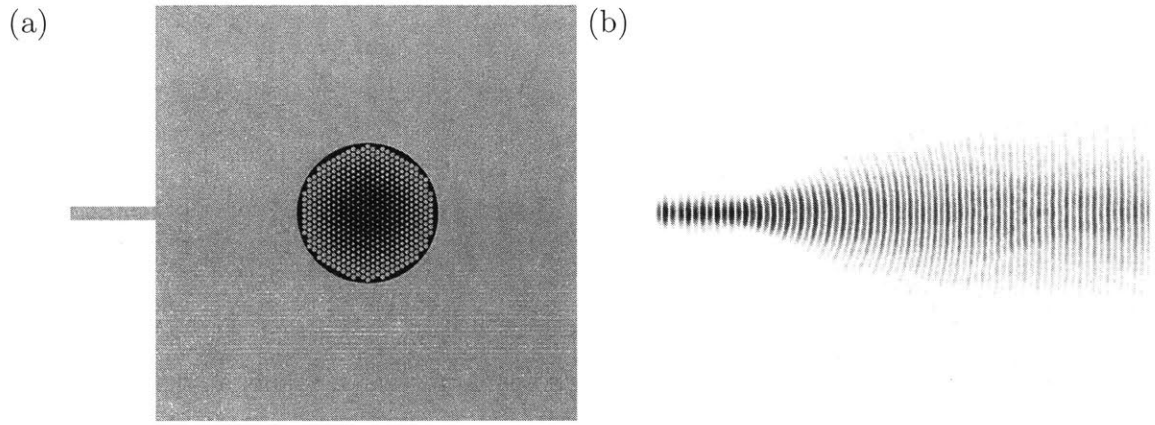


Figure 4.1: (a) Permittivity profile of the 2D simulation in MEEP. Black is a-Si, grey is SiN, and white is $SiO_2$. (b) Resulting magnetic field, $H_z$ of the MEEP simulation.

The permittivity profile of the simulation along with the resulting magnetic field $H_z$ are shown in Figure 4.1 for a lens with radius $R = 5\,\mu m$. This small size is chosen to display the photonic crystal structure in the lens. We can see from the $H_z$ profile that the waveguide mode spreads after it enters the waveguide slab, passes through the lens, and is collimated on the other side of the lens. There is some energy that does not impinge on the lens and thus does not get collimated. Additionally, there appears to be diffraction of the electromagnetic field in and around the lens due to the small size of the lens, but these effects become insignificant as the lens size increases.

The far field is calculated in MEEP by using a Fourier transform to extend the fields out 1 m from the edge of the simulation along all 4 boundaries of the simulation. This is far enough such that any Gaussian beam with a waist size equal to the lens radius we are simulating reaches the far field, allowing us to measure the far field beam divergence accurately. A polar plot of the farfield of a lens with radius $R = 30\,\mu m$ is shown in Figure 4.2(a), where the angle $\theta = 0°$ is aligned with the $x$-axis. The farfield is normalized to the

maximum power. We can see that most of the energy is in the main lobe, demonstrating collimation of the lens.

(a) (b)

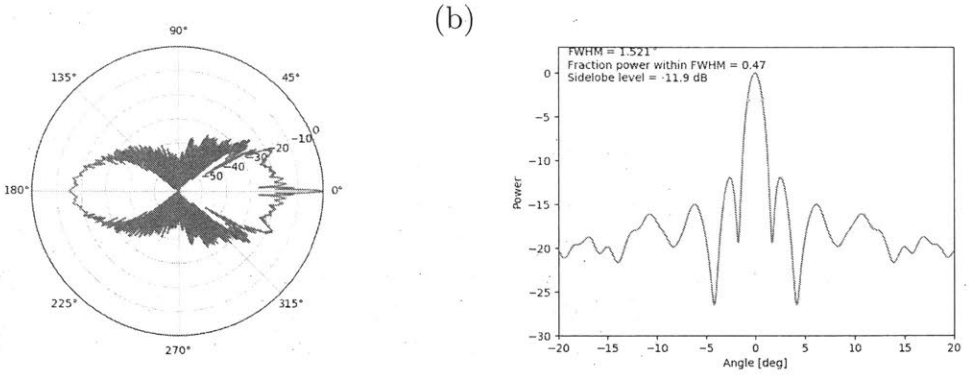


Figure 4.2: Farfield plots for a lens with radius $R = 30\,\mu\text{m}$. (a) Polar plot of the farfield in the SiN slab. (b) Farfield corrected for air and zoomed into the main lobe.

The background and boundaries of the simulation are in the SiN slab. However, we want to know how the beam behaves when it exits the chip into air. Thus, we correct for this using Snell's Law by multiplying the angle of the farfield plot by the effective refractive index of SiN. A farfield plot corrected for air and zoomed into the main lobe is shown in Figure 4.2(b). To measure the degree of collimation of the outgoing beam from the lens, we use the -3dB farfield beamwidth, also known as the full-width half-max (FWHM), as our primary figure of merit. The FWHM is proportional to the beam divergence and gives us a measure of how well collimated the beam is and thus the resolution of beam steering that can be achieved. The remainder of the farfield plots shown in this thesis are corrected for air.

# Chapter 5

# Results

## 5.1 Lens Performance

There are three assumptions that we made when designing the lens: (1) the size of the lens is sufficiently larger than the wavelength of light such that we can approximate the light as rays (which is how the semi-analytical formulation of the Luneburg lens was derived), (2) the rays are emanating from a point source, and (3) the gradient-index lens is sufficiently realized by the photonic crystal. For reference, we simulate an "idealized lens" with the exact desired index of refraction at each point in the lens without discretization from a metamaterial or photonic crystal. The idealized lens achieves a true gradient index and fulfills our third assumption so that we can examine the first two assumptions in isolation.

To examine the first assumption, I run the lens setup "in reverse" using the idealized lens, in which I send a plane wave from the $+x$ direction onto the idealized lens and analyze how the lens focuses the energy. This setup is shown in Figure 5.1 where we can see from the field profile and the energy profile that the wave is focused into a tight spot. The time-averaged energy density is calculated by $\mu_0|\mathbf{H}|^2/2$, where $\mathbf{H}$ is the complex magnetic field.

The focal length of the lens is measured by calculating the location of the maximum in the magnetic field energy density. The error in the measured focal length relative to the

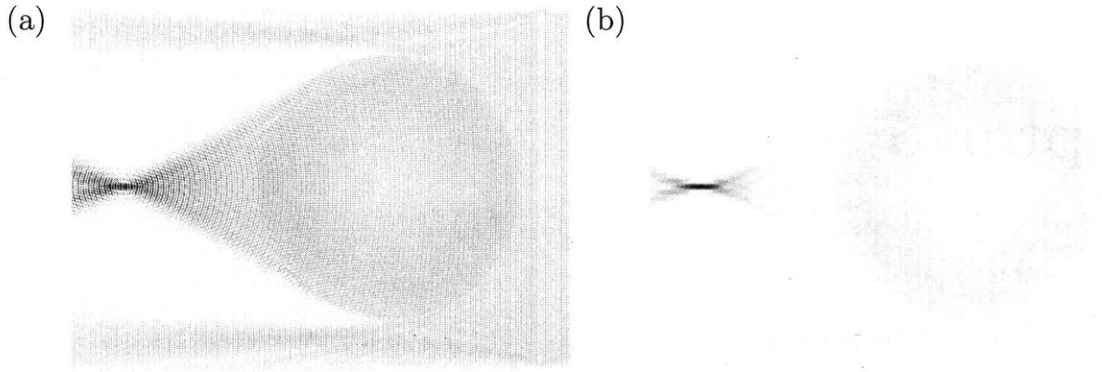


Figure 5.1: Simulation of the lens (gray) with a plane wave sent in from the right so that we can see focusing. (a) $H_z$ profile (red and blue). (b) Time-averaged magnetic field energy density, $\mu_0|\mathbf{H}|^2/2$ (orange).

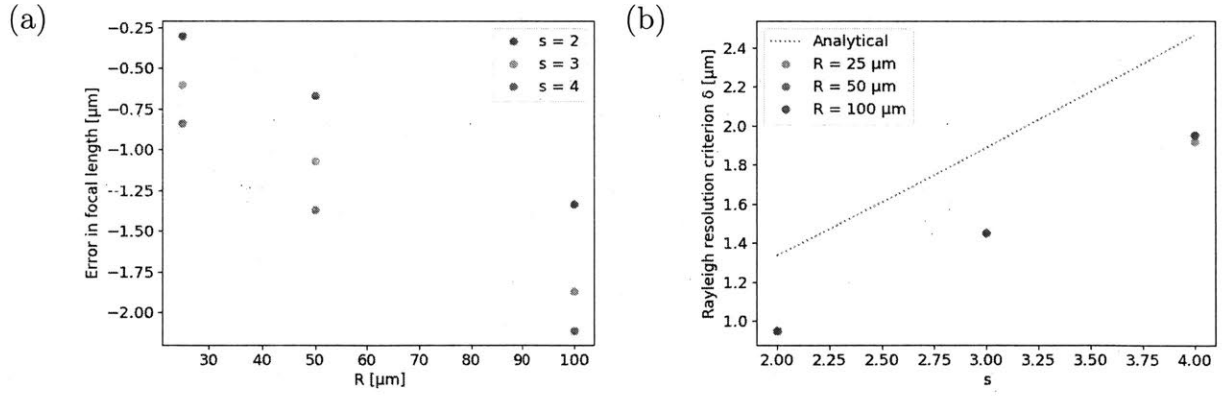


Figure 5.2: Results of sending in a plane wave into the lens and measuring the focused field. (a) Error in the focal length measured by the location of the maximum field. (b) Resolution criterion of the focused field as measured by the distance from the maximum field to the first minimum, $\delta$, and the analytical solution for the Rayleigh diffraction limit. The points for $R = 50\,\mu\text{m}$ and $R = 100\,\mu\text{m}$ are overlayed on each other and thus cannot be seen separately.

designed focal length is plotted in Figure 5.2(a) for various $R$ and $s$. Surprisingly, despite our expectations of smaller diffraction effects for larger lenses, the error appears to increase for larger lenses, which is an area for further investigation. However, while the absolute error increases for larger lenses, the error when normalized to the lens radius decreases.

Additionally, at the measured focal length, I take a cross-section of the energy density transverse to the beam propagation direction and measure the Rayleigh resolution criterion, which is the distance from the maximum to the first minimum. The analytical solution for the Rayleigh diffraction limit is:

$$\delta = \frac{0.61\lambda_0}{n \sin\theta}$$

where $\lambda_0 = 1.55\,\mu\text{m}$ is the wavelength in free space, $n = 1.584$ is the effective index inside the SiN slab, and $\theta = \arctan\left(\frac{1}{s}\right)$ is the half-angle of the focused beam. The measured and analytical Rayleigh resolution limits are plotted in Figure 5.2(b). Interestingly, the measured resolution limit is better than the analytical resolution limit. This may be due to the analytical limit assuming a uniformly illuminated aperture which produces a sinc function at the focal point. Implicitly, this also assumes a flat lens. However, the Luneburg lens is not flat and focuses the fields inside the lens, thus resulting in a non-uniform energy profile at the exit aperture of the lens. We can conclude that approximating the light as rays is a valid approach to designing the lens index profile and that the idealized lens is a diffraction-limited system.

To examine the second assumption, I use a dipole source at the point of the idealized len's designed focal lens and analyze how well the beam is collimated. Figure 5.3 shows the permittivity profile of a simulation where a dipole source is placed at the focal point of the lens and the resulting $H_z$ field. The dipole source emits isotropically and the field that impinges on the lens is collimated. As seen in Figure 5.4, the farfield FWHM of the collimated waveguide source is much larger than that of the collimated dipole source, demonstrating that the waveguide does not approximate a point source very well. This is expected as the

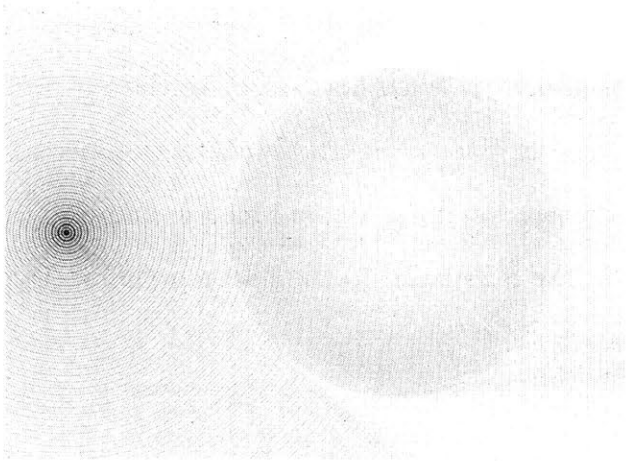

Figure 5.3: $H_z$ (red and blue) overlayed on the permittivity profile (greyscale) of a simulation of a dipole source and an ideal lens with $s = 2$ and $R = 25\,\mu\text{m}$.

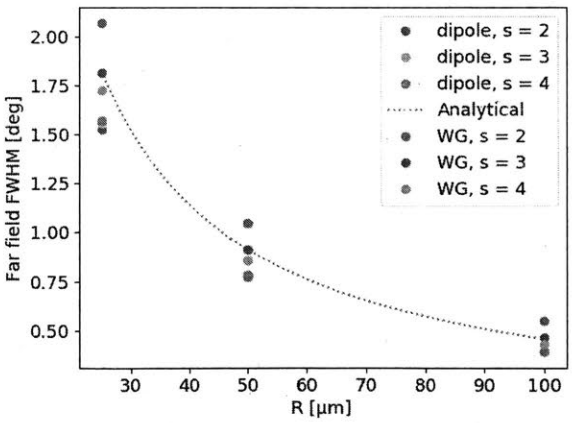


Figure 5.4: Far field FWHM of the collimated beam using an ideal lens and both a dipole source and waveguide (WG) source. The dotted line is the analytical FWHM assuming a uniformly illuminated aperture, which results in a sinc function pattern in the farfield.

waveguide mode has a non-zero width, and this mode propagates in a non-trivial way once it exits the waveguide.

Interestingly, the dipole farfield FWHM is approximately constant as a function of $s$ for a fixed value of $R$, whereas the waveguide farfield FWHM decreases as $s$ increases for a fixed value of $R$. This is because for a small $s$, the waveguide beam does not fully illuminate the lens, decreasing the effective aperture and increasing the farfield FWHM. For larger $s$, the waveguide beam fully illuminates the lens so the lens sees a more uniform source. The tradeoff is that some of the energy from the waveguide may miss the lens, thus increasing losses in the system.

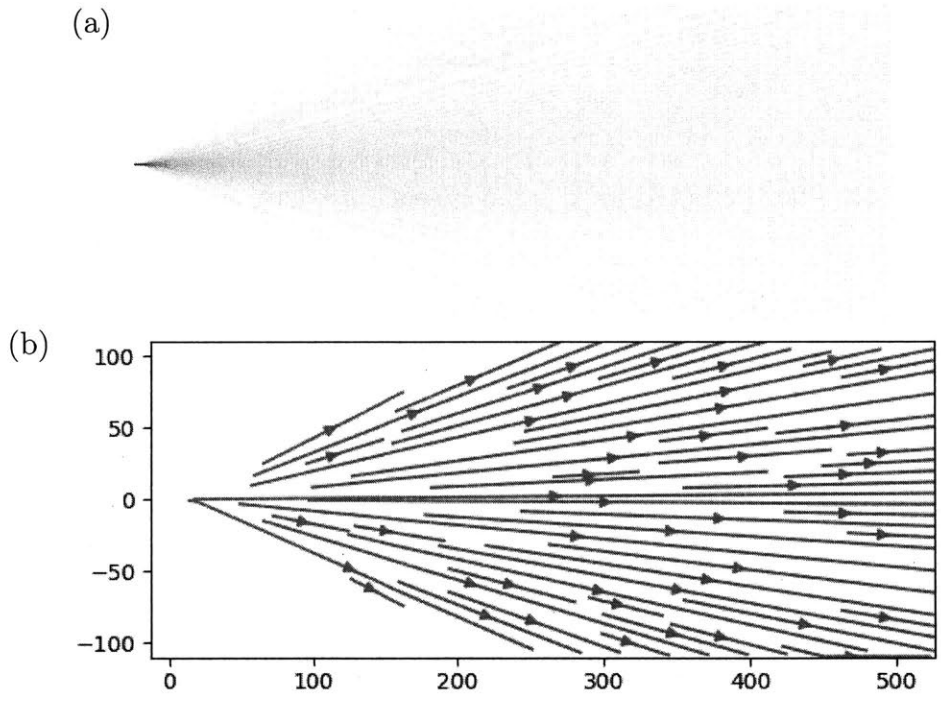


Figure 5.5: Behavior of a waveguide mode traveling from a waveguide into a waveguide slab. (a) $H_z$ (b) Streamlines of the time-averaged Poynting vector, $\mathbf{S}$. Only vectors above an aribtrary threshold are plotted to better visualize the beam in the lab. The point at which the waveguide meets the slab waveguide is at $x = 0$.

To characterize the output from the waveguide, I simulate the waveguide mode as it travels from the waveguide into the slab waveguide without a lens. The time-averaged Poynting vector is calculated as $\mathbf{S} = \frac{1}{2}\Re(\mathbf{E} \times \mathbf{H}^*)$ where $\mathbf{E}$ and $\mathbf{H}$ are the complex electric

and magnetic fields, respectively. The $H_z$ field and a streamline plot of $\mathbf{S}$ are shown in Figure 5.5 which shows the beam spreading as it exits the waveguide. Additionally, the streamline plot contains straight vectors across the entire beam, which suggests that we can approximate the beam using ray optics and find the focal point of these rays.

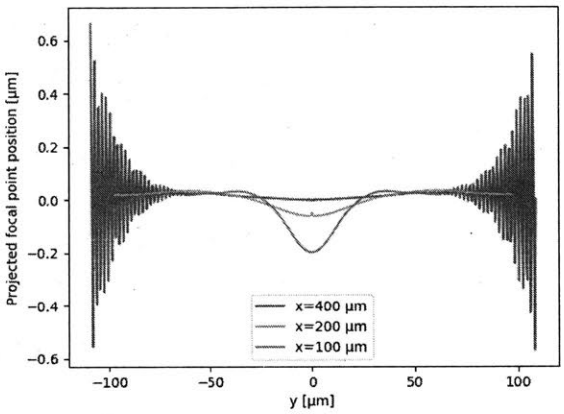


Figure 5.6: The predicted focal point at each $y_i$ along several slices in $x_i$.

At each point in the slab waveguide $(x_i, y_i)$ (in units of μm) where $(x_i = 0, y_i = 0)$ is at the point where the waveguide meets the waveguide slab, we calculate where a ray parallel to $\mathbf{S}$ would intersect the line $y = 0$ which represents the focal point $x_f$:

$$x_f = x_i - \frac{y_i S_x}{S_y}$$

where $S_x$ and $S_y$ are the $x$ and $y$ components of $\mathbf{S}$. This quantity is plotted as a function of $y_i$ for various cuts along the $x$-axis in Figure 5.6. We can see that most of the vectors point away from $x = 0$ as expected. There is a dip at $y = 0$ showing that it does not represent a perfect point source. However, the shift is small so I do not adjust the waveguide position to account for this.

Finally, to examine the final assumption, I simulate the lens constructed with the photonic crystal. Figure 5.7 shows the field results for lenses built using various $a$. For now, we ignore the fabrication constraints on minimum feature size and gap size so that we are not

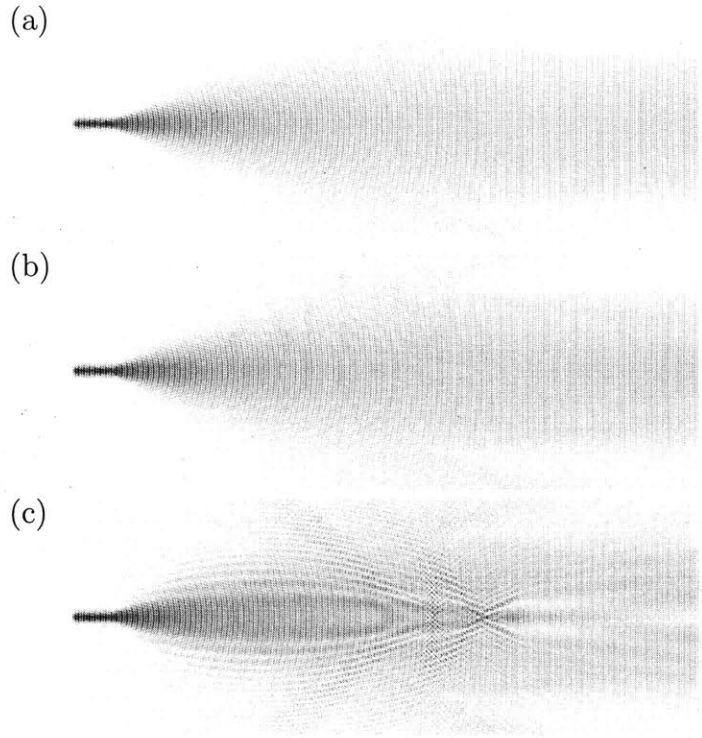


Figure 5.7: Effect of photonic crystal periodicity. Lens simulation with (a) $a = 300\,\text{nm}$, (b) $400\,\text{nm}$, and (c) $500\,\text{nm}$.

truncating the lens index profile. This allows us to separate the effects of discretization and index truncation. For $a = 300\,\text{nm}$, the field looks well-behaved and collimated on the far side of the lens, with the only diffraction being the edge diffraction from the edges of the lens. For $a = 400\,\text{nm}$, there are small signs of diffraction inside the lens, and for $a = 500\,\text{nm}$, the field shows clear signs of diffraction both inside and outside the lens. As previously stated, $a = 500\,\text{nm}$ is above the $\lambda/2$ limit so we would expect to see diffraction effects. Additionally, in the 3D case, this would allow the electromagnetic fields to couple out-of-plane, increasing scattering losses. Because of this, we set $a = 400\,\text{nm}$ to avoid diffractive effects and increase the range of achievable indices compared to $a = 300\,\text{nm}$.

To study the effects of the fabrication constraints, I simulate the photonic crystal lens with the truncated index profile. The far field of the collimated beam using the photonic crystal lens and the idealized lens match very closely, as seen in Figure 5.8. Thus, treating the photonic crystal as a homogeneous medium with an effective refractive index is a suitable

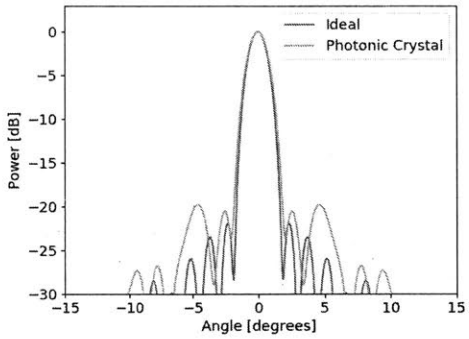


Figure 5.8: Far field of photonic crystal lens and idealized lens for $R = 30\,\mu\text{m}$.

approximation. Additionally, the truncation of the realized $n(r)$ compared to the analytical solution results in a negligible difference in the far-field pattern.

(a)

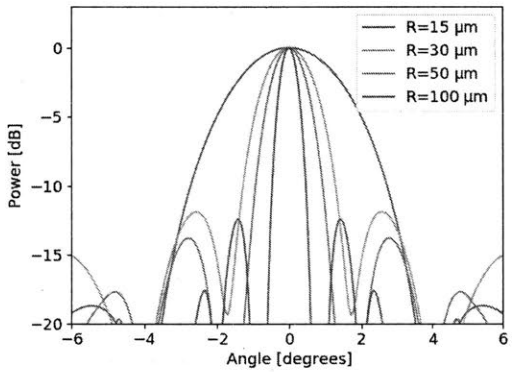


(b)

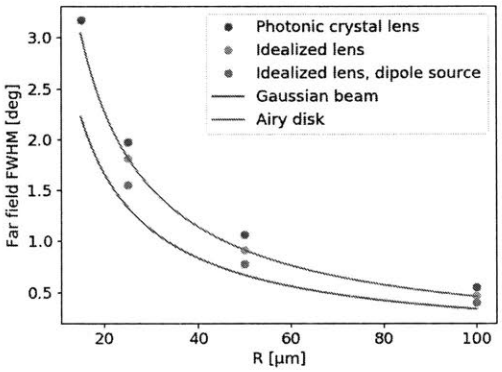


Figure 5.9: (a) Far field of the photonic crystal lens for various radii. (b) FWHM of the photonic crystal lens, idealized lens, and idealized lens illuminated by a dipole source for various lens radii. For reference the analytical FWHM of an Airy disk profile and a Gaussian beam are also plotted.

As seen in Figure 5.9(a), the FWHM is inversely proportional to the lens radius and the level of the sidelobes do not change appreciably. As stated before, this is as expected because the diameter of the lens is equivalent to the aperture size which is inversely proportional to the beam width. In Figure 5.9(b), the far field FWHM is plotted as a function of $R$ for the photonic crystal lens, the idealized lens, and the idealized lens illuminated by a dipole source. For comparison, the expected FWHM assuming an Airy disk profile where the aperture is equal to the lens diameter is plotted as well as the expected FWHM corresponding to a

Gaussian beam where the beam waist is equal to the lens radius. The photonic crystal lens matches the airy disk profile closely. The Gaussian beam represents the upper limit of performance since the Gaussian beam has infinite width in the transverse direction. The far-field FWHM in air is 0.55° for a lens with radius $R = 100\,\text{um}$.

Although the Luneburg lens is circularly symmetric and thus has a theoretical 360° FOV, in practice the FOV is limited by the placement of the waveguides as they may obstruct the beam from other waveguides. Giving a clearance of 4 µm between any particular wavegudie and the collimated beam from any other waveguide, this gives us an effective FOV of 160.5°. Assuming that the waveguide feeds are spaced 4 um apart and that beamwidth is inversely proportional to the lens size, we can extrapolate and predict that a lens with radius $R = 491\,\text{um}$ can accommodate 1024 waveguide ports (corresponding to 1024 resolvable points) where each beam would have a beamwidth of 0.11°.

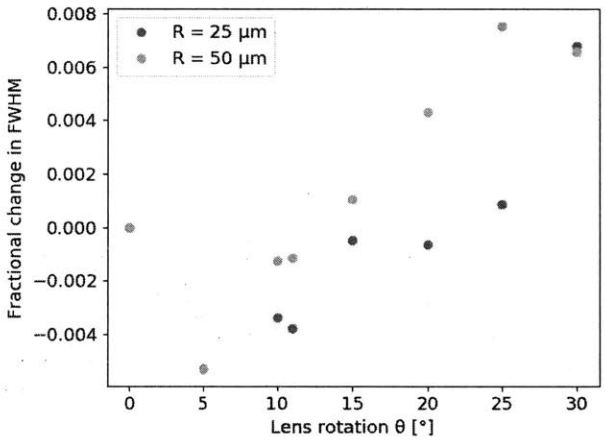


Figure 5.10: Far field of photonic crystal lens as a function of lens rotation.

To confirm the rotational symmetry of the lens, I simulate the lens performance for the lens rotated at various angles. Because of the 6-fold symmetry of the photonic crystal, it is only necessary to simulate lens rotations up to 30°. The results are shown in Figure 5.10 and show that the lens is indeed rotationally symmetric.

## 5.2 Robustness to Fabrication

Although we can theoretically design a lens and analyze its performance given some design, the fabrication processes have some tolerance associated with them and do not necessarily hit the exact geometry that we specify. Ideally, the lens is robust enough to these fabrication variations, which includes thicknesses of the materials and location of deposited material.

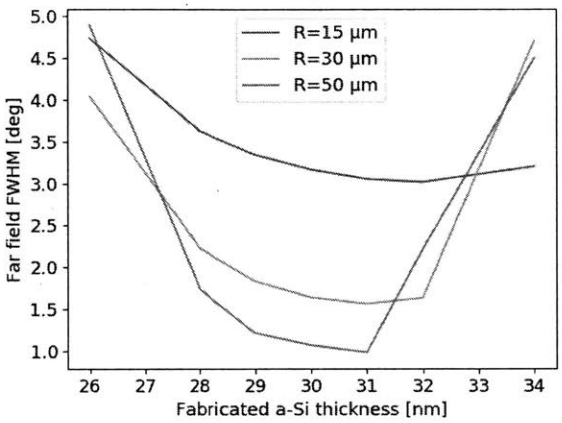


Figure 5.11: Measuring robustness to fabricated a-Si thickness, where the designed a-Si thickness is $t = 30\,\text{nm}$.

The largest source of uncertainty is in the fabricated a-Si thickness. Figure 5.11 shows the FWHM of lenses that vary in the fabricated a-Si thickness using a designed a-Si thickness of $t = 30\,\text{nm}$. We can see that as we increase $R$, the performance improves at the desired thickness, but also gets more sensitive to the fabricated thickness.

For optimization, we can also fix the number of ports and the FOV of a design and optimize $s$ for robustness. Figure 5.12 shows the case for 64 ports spaced $4\,\mu\text{m}$ apart over a 160° arc, thus allowing a 160° FOV. We range $s$ from 2.4 to 3.0, and for each $s$ design the lens radius to accomodate the 64 ports. For $s = 2.4$, the FWHM is dramatically worse because the photonic crystal cannot achieve the required index range. We also note that $s = 2.6$ performs better than $s = 2.8, 3.0$ due to the increased aperture, but is also less robust.

Another source of variation is the a-Si pattern that is fabricated. One way this can manifest itself is through the fabricated hole size. To explore this, I apply independent

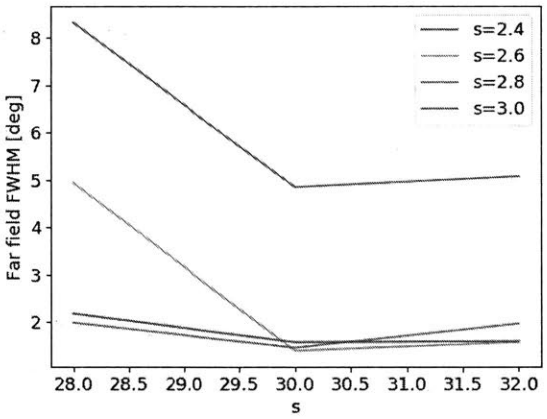


Figure 5.12: Measuring robustness to fabricated a-Si thickness, where the designed a-Si thickness is $t = 30\,\text{nm}$ and there are 64 ports.

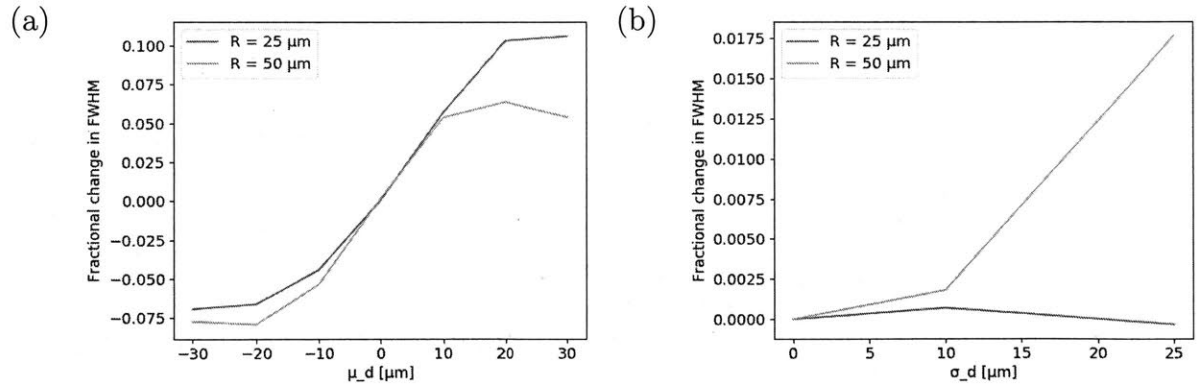


Figure 5.13: Robustness of the lens performance to the hole size by applying Gaussian noise $\epsilon_d \sim \mathcal{N}(\mu_d, \sigma_d)$ to the hold size as $d' = d + \epsilon$. This is measured fractional change of the FWHM with respect to the unperturbed lens as a function of (a) $\mu_d$ for $\sigma_d = 10$ (the dotted line represent the case where $\mu_d =$ and $\sigma = 0$ and (b) $\sigma_d$ for $\mu_d = 0$.

Gaussian noise to each hole size, $d' = d + \epsilon_d$ where $\epsilon_d \sim \mathcal{N}(\mu_d, \sigma_d)$ and $\mu_d$ and $\sigma_d$ are the mean and standard deviation of the Gaussian noise, respectively. The FWHM results are shown in Figure 5.13. Figure 5.13(a) varies $\mu_d$ while fixing $\sigma_d = 10$ which is valid because the variations in hole sizes are likely to be strongly correlated in the fabrication if the mask is under- or over-exposed. We can see that the FWHM varies by $\sim 10\%$ and actually decreases for negative values of $\mu_d$. This implies that the lens is not perfectly optimized and agrees with the results in Figure 5.11 as both decreasing the hole size $d$ and increasing a-Si thickness $t$ results in a higher lens index.

Figure 5.13(a) varies $\sigma_d$ and shows that the lens performance is rather robust with respect to random perturbations in the hole size. This is likely because locally the perturbations tend to cancel each other out so that the mean index is still equal to the originally desired index.

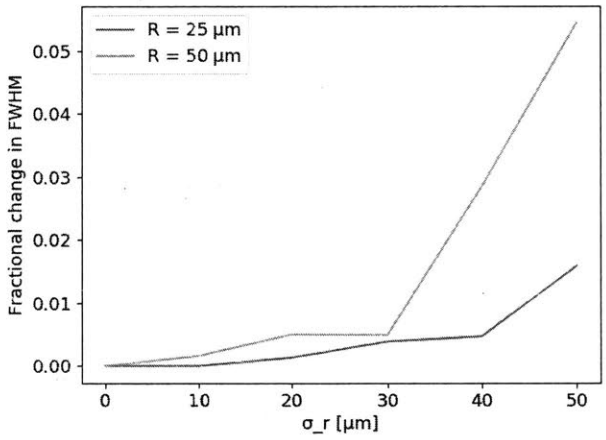


Figure 5.14: Robustness of the lens performance to the hole location by applying Gaussian noise $\epsilon_r \sim \mathcal{N}(\mu_r, \sigma_r)$ to the coordinates of each hole as $x' = x + \epsilon_r$ and $y' = y + \epsilon_r$. Set $\mu_r = 0$. This is measured as the fractional change of the FWHM with respect to the unperturbed lens.

Another way that variations in the fabrication pattern can manifest itself is through the hole position. I apply independent Gaussian noise to the coordinates of each hole, $x' = x + \epsilon_r$ and $y' = y + \epsilon_r$ where $\epsilon_r \sim \mathcal{N}(\mu_r, \sigma_r)$ and $\mu_r$ and $\sigma_r$ are the mean and standard deviation of the Gaussian noise, respectively. The results are shown in Figure 5.14 for the case where

$\mu_r = 0$ ($\mu_r \neq 0$ is just equivalent to shifting the entire lens). The lens performance is robust to variations in the hole location as the FWHM only deviates by 1.5% for $\sigma_r = 50\,\mu\text{m}$ and $R = 25\,\mu\text{m}$. As before, this can be explained by perturbations cancelling each other out so that the propagating beam still sees the mean index in the lens.

# Chapter 6

# Conclusion and Outlook

In summary, I have proposed a circularly symmetric lens based on the Luneburg lens design. The gradient index is realized with a photonic crystal that is subject to CMOS-compatiable fabrication constraints. Simulations show that the lens can achieve a FWHM in the farfield of 0.55° and that this is expected to scale inversely with the lens size. Additionally, the lens was tested for robustness to fabrication variations including a-Si thickness and fabricated a-Si pattern. The lens can enable wide-angle optical beam steering with circularly-symmetric performance (including beamwidth, sidelobe level, and power efficiency) with an FOV of 160°. This solid-state optical beam steering design could enable inexpensive, robust, and miniaturized LIDAR sensors and optical communication devices.

There are several aspects in which the lens performance can be improved. It is clear that the lens is not perfectly optimized and may either have a different focal length than expected and that the point of divergence cannot be assumed to be at the edge of the waveguide. A simple way to adjust for this would be to optimize the waveguide placement and/or an offset to the hole sizes. Another path would be to use Hamiltonian ray optics for fast simulations and numerically optimize over the lens profile to take into account the non-point nature of the waveguide source. For the highest degree of accuracy, optimization methods could be used on the lens's sub-wavelength structure directly through full-wave simulations, although

this would be extremely computationally expensive and likely reserved for the last stage of optimization to fine-tune the local optima.

Some potential future directions for this project include studying different fabrication processes and material stacks to see how the lens should be optimized differently. For example, the loss in a-Si is one of the limiting factors of the efficiency of the previous system, so one could use a different material or even pattern SiN directly. In addition, while the previous design was fabricated using low pressure chemical vapor deposition, other techniques such as electron beam lithography can achieve much greater fabrication resolutions and can thus relax many of the fabrication constraints, allowing for a greater range of lens designs that may be more robust or higher-performing. Finally, while this architecture for optical beam steering is composed of numerous components that work together (e.g., switch tree, waveguides, collimating lens, and grating), one could imagine a photonic crystal to combine the functionality of multiple elemnts, such as a device that collimates the beam and directs it out-of-plane at the same time to replace the lens and the grating.

# References


[1] H. D. Tholl, "Novel laser beam steering techniques," vol. 6397, p. 639708, International Society for Optics and Photonics, sep 2006.

[2] M. J. R. Heck, "Highly integrated optical phased arrays: photonic integrated circuits for optical beam shaping and beam steering," *Nanophotonics*, vol. 6, no. 1, pp. 93–107, 2017.

[3] C. V. Poulton, A. Yaacobi, D. B. Cole, M. J. Byrd, M. Raval, D. Vermeulen, and M. R. Watts, "Coherent solid-state lidar with silicon photonic optical phased arrays," *Optics letters*, vol. 42, no. 20, pp. 4091–4094, 2017.

[4] F. Aflatouni, B. Abiri, A. Rekhi, and A. Hajimiri, "Nanophotonic projection system," *Optics Express*, vol. 23, p. 21012, aug 2015.

[5] K. Zhang, J. Yan, and S.-C. Chen, "Automatic construction of building footprints from airborne lidar data," *IEEE Transactions on Geoscience and Remote Sensing*, vol. 44, no. 9, pp. 2523–2533, 2006.

[6] A. Schumann, D. Arndt, T. Wiatr, A. E. Götz, and A. Hoppe, "High-resolution terrestrial laser scanning and 3d modelling of a mineral deposit for extraction management optimisation [hochauflösendes terrestrisches laserscanning und 3d-modellierung einer kalklagerstätte zur optimierung des abbaumanagements]," *Zeitschrift der Deutschen Gesellschaft für Geowissenschaften*, vol. 162, no. 4, pp. 435–442, 2011.

[7] U. Weiss and P. Biber, "Plant detection and mapping for agricultural robots using a 3d lidar sensor," *Robotics and autonomous systems*, vol. 59, no. 5, pp. 265–273, 2011.

[8] A. F. Chase, D. Z. Chase, J. F. Weishampel, J. B. Drake, R. L. Shrestha, K. C. Slatton, J. J. Awe, and W. E. Carter, "Airborne lidar, archaeology, and the ancient maya landscape at caracol, belize," *Journal of Archaeological Science*, vol. 38, no. 2, pp. 387–398, 2011.

[9] G. L. Heritage, A. R. Large, and M. Charlton, *Laser scanning for the environmental sciences*. Wiley Online Library, 2009.

[10] B. Schwarz, "Lidar: Mapping the world in 3d," *Nature Photonics*, vol. 4, no. 7, p. 429, 2010.

[11] A. Kasturi, V. Milanovic, B. H. Atwood, and J. Yang, "Uav-borne lidar with mems mirror-based scanning capability," in *Laser Radar Technology and Applications XXI*, vol. 9832, p. 98320M, International Society for Optics and Photonics, 2016.

[12] S. Arnon, S. Rotman, and N. S. Kopeika, "Beam width and transmitter power adaptive to tracking system performance for free-space optical communication," *Applied optics*, vol. 36, no. 24, pp. 6095–6101, 1997.

[13] S. R. Davis, S. D. Rommel, D. Gann, B. Luey, J. D. Gamble, M. Ziemkiewicz, and M. Anderson, "A lightweight, rugged, solid state laser radar system enabled by non-mechanical electro-optic beam steerers," vol. 9832, p. 98320K, International Society for Optics and Photonics, may 2016.

[14] B. Löfving and S. Hård, "Beam steering with two ferroelectric liquid-crystal spatial light modulators," *Optics Letters*, vol. 23, p. 1541, oct 1998.

[15] S. A. Khan and N. A. Riza, "Demonstration of 3-dimensional wide angle laser beam scanner using liquid crystals," *Optics Express*, vol. 12, p. 868, mar 2004.

[16] P. McManamon, T. Dorschner, D. Corkum, L. Friedman, D. Hobbs, M. Holz, S. Liberman, H. Nguyen, D. Resler, R. Sharp, and E. Watson, "Optical phased array technology," *Proceedings of the IEEE*, vol. 84, pp. 268–298, feb 1996.

[17] M. R. M. Hashemi, S.-H. Yang, T. Wang, N. Sepúlveda, and M. Jarrahi, "Electronically-Controlled Beam-Steering through Vanadium Dioxide Metasurfaces," *Scientific Reports*, vol. 6, p. 35439, dec 2016.

[18] A. Tuantranont, V. Bright, J. Zhang, W. Zhang, J. Neff, and Y. Lee, "Optical beam steering using mems-controllable microlens array," *Sensors and Actuators A: Physical*, vol. 91, no. 3, pp. 363–372, 2001.

[19] H. W. Yoo, N. Druml, D. Brunner, C. Schwarzl, T. Thurner, M. Hennecke, and G. Schitter, "Mems-based lidar for autonomous driving," *e & i Elektrotechnik und Informationstechnik*, pp. 1–8, 2018.

[20] U. Hofmann, F. Senger, F. Soerensen, V. Stenchly, B. Jensen, and J. Janes, "Biaxial resonant 7mm-mems mirror for automotive lidar application," in *Optical MEMS and Nanophotonics (OMN), 2012 International Conference on*, pp. 150–151, IEEE, 2012.

[21] U. Krishnamoorthy, K. Li, K. Yu, D. Lee, J. Heritage, and O. Solgaard, "Dual-mode micromirrors for optical phased array applications," *Sensors and Actuators A: Physical*, vol. 97-98, pp. 21–26, apr 2002.

[22] "MEMS tip/tilt and piston mirror arrays as diffractive optical elements," vol. 5894, p. 58940C, International Society for Optics and Photonics, aug 2005.

[23] K. Inagaki and Y. Karasawa, "Ultrahigh-speed optical-beam steering by optical phased array antenna," vol. 2699, p. 210, International Society for Optics and Photonics, apr 1996.

[24] A. Yaacobi, J. Sun, M. Moresco, G. Leake, D. Coolbaugh, and M. R. Watts, "Integrated phased array for wide-angle beam steering," *Optics letters*, vol. 39, no. 15, pp. 4575–4578, 2014.

[25] D. N. Hutchison, J. Sun, J. K. Doylend, R. Kumar, J. Heck, W. Kim, C. T. Phare, A. Feshali, and H. Rong, "High-resolution aliasing-free optical beam steering," *Optica*, vol. 3, no. 8, pp. 887–890, 2016.

[26] T. Komljenovic, R. Helkey, L. Coldren, and J. E. Bowers, "Sparse aperiodic arrays for optical beam forming and LIDAR," *Optics Express*, vol. 25, p. 2511, feb 2017.

[27] J. K. Doylend, M. J. R. Heck, J. T. Bovington, J. D. Peters, L. A. Coldren, and J. E. Bowers, "Two-dimensional free-space beam steering with an optical phased array on silicon-on-insulator," *Optics Express*, vol. 19, p. 21595, oct 2011.

[28] D. Inoue, T. Ichikawa, A. Kawasaki, and T. Yamashita, "Demonstration of a new optical scanner using silicon photonics integrated circuit," *Optics Express*, vol. 27, p. 2499, feb 2019.

[29] H. Ito, Y. Kusunoki, D. Akiyama, R. Tetsuya, H. Abe, and T. Baba, "Enhanced light emission from a Si photonics beam steering device consisting of asymmetric photonic crystal waveguide," in *Silicon Photonics XIV* (G. T. Reed and A. P. Knights, eds.), vol. 10923, p. 37, SPIE, mar 2019.

[30] S. A. Skirlo, *Photonics for technology: circuits, chip-scale LIDAR, and optical neural networks.* PhD thesis, Massachusetts Institute of Technology, 2017.

[31] J. J. López, S. A. Skirlo, D. Kharas, J. Sloan, J. Herd, P. Juodawlkis, M. Soljačić, and C. Sorace-Agaskar, "Planar-lens enabled beam steering for chip-scale lidar," in *CLEO: Science and Innovations*, pp. SM3I–1, Optical Society of America, 2018.

[32] M. Laikin, "Wide angle lens systems," in *1980 International Lens Design Conference*, vol. 237, pp. 530–534, International Society for Optics and Photonics, 1980.

[33] R. K. Luneburg and M. Herzberger, *Mathematical theory of optics.* Univ of California Press, 1964.

[34] S. P. Morgan, "General solution of the luneberg lens problem," *Journal of Applied Physics*, vol. 29, no. 9, pp. 1358–1368, 1958.

[35] W. Southwell, "Index profiles for generalized luneburg lenses and their use in planar optical waveguides," *JOSA*, vol. 67, no. 8, pp. 1010–1014, 1977.

[36] H. Mosallaei and Y. Rahmat-Samii, "Nonuniform Luneburg and two-shell lens antennas: radiation characteristics and design optimization," *IEEE Transactions on Antennas and Propagation*, vol. 49, no. 1, pp. 60–69, 2001.

[37] J. Sanford, "Scattering by spherically stratified microwave lens antennas," *IEEE Transactions on Antennas and Propagation*, vol. 42, pp. 690–698, may 1994.

[38] G. Peeler and H. Coleman, "Microwave stepped-index luneberg lenses," *IRE Transactions on Antennas and Propagation*, vol. 6, pp. 202–207, apr 1958.

[39] L. C. Gunderson and G. T. Holmes, "Microwave Luneburg Lens," *Applied Optics*, vol. 7, p. 801, may 1968.

[40] B. Fuchs, L. Le Coq, O. Lafond, S. Rondineau, and M. Himdi, "Design Optimization of Multishell Luneburg Lenses," *IEEE Transactions on Antennas and Propagation*, vol. 55, pp. 283–289, feb 2007.

[41] H. F. Ma, B. G. Cai, T. X. Zhang, Y. Yang, Jiang, and Cui, "Three-Dimensional Gradient-Index Materials and Their Applications in Microwave Lens Antennas," *IEEE Transactions on Antennas and Propagation*, vol. 61, pp. 2561–2569, may 2013.

[42] V. E. Wood, D. T. Moore, W. H. Southwell, C. B. Wooley, and J. R. Busch, "Rectangular Luneburg-type lenses for integrated optics," *Optics Letters*, vol. 8, p. 226, apr 1983.

[43] F. Zernike, "Luneburg lens for optical waveguide use," *Optics Communications*, vol. 12, pp. 379–381, dec 1974.

[44] S. K. Yao and D. B. Anderson, "Shadow sputtered diffraction-limited waveguide Luneburg lenses," *Applied Physics Letters*, vol. 33, pp. 307–309, aug 1978.

[45] S. K. Yao, D. B. Anderson, R. R. August, B. R. Youmans, and C. M. Oania, "Guided-wave optical thin-film Luneburg lenses: fabrication technique and properties," *Applied Optics*, vol. 18, p. 4067, dec 1979.

[46] L. H. Gabrielli and M. Lipson, "Integrated Luneburg lens via ultra-strong index gradient on silicon," *Optics Express*, vol. 19, p. 20122, oct 2011.

[47] A. Di Falco, S. C. Kehr, and U. Leonhardt, "Luneburg lens in silicon photonics," *Optics Express*, vol. 19, p. 5156, mar 2011.

[48] F. Gaufillet and E. Akmansoy, "Graded Photonic Crystals for Luneburg Lens," *IEEE Photonics Journal*, vol. 8, pp. 1–11, feb 2016.

[49] Y.-Y. Zhao, Y.-L. Zhang, M.-L. Zheng, X.-Z. Dong, X.-M. Duan, and Z.-S. Zhao, "Anisotropic and omnidirectional focusing in Luneburg lens structure with gradient photonic crystals," *Journal of Optics*, vol. 19, p. 015605, jan 2017.

[50] B. Vasic, G. Isic, R. Gajic, and K. Hingerl, "Controlling electromagnetic fields with graded photonic crystals in metamaterial regime," *Optics Express*, vol. 18, p. 20321, sep 2010.

[51] H. Gao, B. Zhang, S. G. Johnson, and G. Barbastathis, "Design of thin–film photonic metamaterial Lüneburg lens using analytical approach," *Optics Express*, vol. 20, p. 1617, jan 2012.

[52] X.-H. Sun, Y.-L. Wu, W. Liu, Y. Hao, and L.-D. Jiang, "Luneburg lens composed of sunflower-type graded photonic Crystals," *Optics Communications*, vol. 315, pp. 367–373, mar 2014.

[53] S. Takahashi, C.-h. Chang, S. Y. Yang, and G. Barbastathis, "Design and fabrication of dielectric nanostructured luneburg lens in optical frequencies," in *Optical MEMS and Nanophotonics (OPT MEMS), 2010 International Conference on*, pp. 179–180, IEEE, 2010.

[54] P. Muñoz, G. Micó, L. A. Bru, D. Pastor, D. Pérez, J. D. Doménech, J. Fernández, R. Baños, B. Gargallo, R. Alemany, A. M. Sánchez, J. M. Cirera, R. Mas, and C. Domínguez, "Silicon Nitride Photonic Integration Platforms for Visible, Near-Infrared and Mid-Infrared Applications.," *Sensors (Basel, Switzerland)*, vol. 17, sep 2017.

[55] D. J. Blumenthal, R. Heideman, D. Geuzebroek, A. Leinse, and C. Roeloffzen, "Silicon Nitride in Silicon Photonics," *Proceedings of the IEEE*, vol. 106, pp. 2209–2231, dec 2018.

[56] "Broadband mid-infrared frequency comb generation in a Si_3N_4 microresonator," *Optics Letters*, vol. 40, p. 4823, nov 2015.

[57] D. T. Pierce and W. E. Spicer, "Electronic Structure of Amorphous Si from Photoemission and Optical Studies," *Physical Review B*, vol. 5, pp. 3017–3029, apr 1972.

[58] D. R. Smith, S. Schultz, P. Markoš, and C. Soukoulis, "Determination of effective permittivity and permeability of metamaterials from reflection and transmission coefficients," *Physical Review B*, vol. 65, no. 19, p. 195104, 2002.

[59] D. Smith, D. Vier, T. Koschny, and C. Soukoulis, "Electromagnetic parameter retrieval from inhomogeneous metamaterials," *Physical review E*, vol. 71, no. 3, p. 036617, 2005.

[60] R. A. Shelby, D. R. Smith, and S. Schultz, "Experimental verification of a negative index of refraction," *science*, vol. 292, no. 5514, pp. 77–79, 2001.

[61] J. D. J. D. Joannopoulos, *Photonic crystals : molding the flow of light.* Princeton University Press, 2008.

[62] H. Kosaka, T. Kawashima, A. Tomita, M. Notomi, T. Tamamura, T. Sato, and S. Kawakami, "Self-collimating phenomena in photonic crystals," *Applied Physics Letters*, vol. 74, p. 1212, feb 1999.

[63] H. Kosaka, T. Kawashima, A. Tomita, M. Notomi, T. Tamamura, T. Sato, and S. Kawakami, "Superprism phenomena in photonic crystals," *Physical review B*, vol. 58, no. 16, p. R10096, 1998.

[64] A. F. Oskooi, D. Roundy, M. Ibanescu, P. Bermel, J. Joannopoulos, and S. G. Johnson, "Meep: A flexible free-software package for electromagnetic simulations by the FDTD method," *Computer Physics Communications*, vol. 181, pp. 687–702, mar 2010.

[65] M. Dupré, L. Hsu, and B. Kanté, "On the design of random metasurface based devices," *Scientific reports*, vol. 8, no. 1, p. 7162, 2018.

[66] S. Johnson and J. Joannopoulos, "Block-iterative frequency-domain methods for Maxwell's equations in a planewave basis," *Optics Express*, vol. 8, p. 173, jan 2001.